

## Searching for Cosmic Birefringence with the BICEP3 Polarimeter

JAMES A. CORNELISON<sup>1</sup>

<sup>1</sup>*Harvard-Smithsonian Center for Astrophysics 60 Garden Street MS 42, Cambridge, MA 02138, USA*

### ABSTRACT

Conservation of parity in the electromagnetic force is a part of the foundation of all modern physics. However, unification of the electromagnetic and weak forces at high energies implies that, like its weak counterpart, the electromagnetic force may also violate parity conservation. It has been shown that adding a parity violating Chern-Simons term to the electromagnetic Lagrangian could physically manifest as a uniform axial rotation of plane polarization which would result in non-zero  $EB$  and  $TB$  correlations in CMB cross spectra. Using a EB/TB-minimization technique on two year-long BICEP3 CMB observations spanning 2017 and 2018, a uniform polarization rotation of  $\Delta\psi = -0.44 \pm 0.12^\circ(\text{stat})$  and  $\Delta\psi = -0.40 \pm 0.12^\circ(\text{stat})$  is estimated respectively. This rotation is degenerate with instrumental effects, however, and so the co-polar axes of a CMB experiment must be precisely calibrated in order to be able probe for such an effect. Observations of a finely polarized thermal source in January 2018 were used to measure the uniform polarization offset of the BICEP3 polarimeter to be  $\bar{\phi}_Q = -1.15 \pm 0.04^\circ(\text{stat}) \pm 1.61^\circ(\text{sys})$  for both observing seasons, which yield estimates on uniform polarization rotation from Cosmic Birefringence to be  $\alpha = 0.71 \pm 0.13^\circ(\text{stat}) \pm 1.61^\circ(\text{sys})$  and  $\alpha = 0.75 \pm 0.13^\circ(\text{stat}) \pm 1.61^\circ(\text{sys})$ . Due

Corresponding author: James Cornelison  
[james\\_cornelison@g.harvard.edu](mailto:james_cornelison@g.harvard.edu)

primarily to the systematic uncertainties, these measurements are on the level of the best ground-based measurements to-date, but not the space-based measurement made by *Planck*. The source of the dominating systematic uncertainties is known, however, and future work on mitigating systematics could improve our uncertainties to be well below that of *Planck*.

*Keywords:* Cosmic Microwave Background, Cosmic Birefringence, Absolute Polarization Calibration

## 1. INTRODUCTION

Throughout the development of the framework that today is known as the Standard Model assumptions were made about certain symmetries of physical properties. Assumptions of symmetry in charge conjugation, parity, and time-reversal were initially driven both by a lack of evidence to the contrary and also a certain elegance and simplicity in the mathematics that these assumptions facilitated. In contemporary physics, however, it has been well-established that charge and parity symmetries (CP) are violated in certain circumstances, particularly in weak interactions ([Lee & Yang 1956](#))([Wu et al. 1957](#)).

While evidence of CP-violations are found only in weak interactions to-date, the fact that the electromagnetic and weak forces are related through the electroweak force suggests that the electromagnetic force may also be CP-violating. Some theoretical frameworks have been constructed to predict observable phenomena resulting from electromagnetic CP-violations, particularly, in the context of this paper, manifesting as a birefringence between the propagation of two oppositely circularly polarized photons due to parity asymmetry ([Carroll et al. 1990](#)). In the case of parity violation in the electromagnetic force, the disparity between two oppositely circularly polarized photons would be largest in sources at the farthest observable distances in the universe, namely high-redshift galaxies and the Cosmic Microwave Background (CMB). In addition to their primary science objectives, numerous CMB experiments over the past decade have attempted to detect birefringent signals with

increasing precision. With no clear detection yet, the upper limit on Cosmic Birefringence is slowly decreasing.

This paper describes the use of a Rotating Polarized Source in conjunction with the BICEP3 polarimeter, an instrument dedicated to measuring CMB polarization with unparalleled precision, to search for signals of parity violations in the electromagnetic force by precisely measuring the polarization properties of the instrument in order to differentiate between instrumental effects and birefringent effects due to parity violations. The paper is separated into three major parts: The rest of Section 1 elaborates on the physics of Cosmic Birefringence, its impact on signals from the CMB, and also gives a brief overview of the BICEP3 instrument. Sections 2 to 4 describes a Rotating Polarized Source (RPS) and analyzes the observations of which were taken with BICEP3 to determine the instrument’s polarization properties. Section 6 analyzes real preliminary CMB data from BICEP3 to acquire a measure of the uniform polarization rotation. Lastly, Section 7 compares CMB-derived results to the RPS-derived results acquired in the previous sections to establish a new upper limit on Cosmic Birefringence.

### 1.1. *Cosmic Birefringence*

Conservation of parity is part of the foundation for all of modern physics. However, it has been found that conservation of parity is violated in some interactions that involve the weak force (Lee & Yang 1956)(Wu et al. 1957). Unification of the electromagnetic and weak forces at high energies suggests that the electromagnetic force may violate parity conservation as well. Additions to the theoretical framework of modern physics have been investigated in order to hypothesize the characteristics of observables in scenarios where parity is not conserved in electromagnetism. The Chern-Simons Lagrangian is one such example in which parity symmetry is violated (Carroll et al. 1990). Interactions between a photon,  $\gamma$ , and a coupling four-vector,  $p_\mu$ , can be written as:

$$\mathcal{L}_p = -\frac{1}{4}F_{\mu\nu}F^{\mu\nu} - \frac{1}{2}p_\alpha A_\beta \tilde{F}^{\alpha\beta} \quad (1)$$

Where  $\tilde{F}^{\alpha\beta}$  is the dual electromagnetic tensor

$$\tilde{F}^{\alpha\beta} = \frac{1}{2}\epsilon^{\alpha\beta\mu\nu}F_{\mu\nu} \quad (2)$$

Physically,  $p$ , can be thought of as a mass term ( $p_\mu p^\mu = -m^2$ ) and (Carroll et al. 1990) shows that such an interaction manifests as birefringence in which left- and right-circularly polarized light travel at different velocities.

$$\omega^2 - k^2 = \pm (p_0 k - \omega p \cos \theta) \left[ 1 - \frac{p^2 \sin^2 \theta}{\omega^2 - k^2} \right]^{1/2} \quad (3)$$

where  $\theta$  is the angle between spacial vector  $\vec{p}$  and wave vector  $\vec{k}$  and  $p = |\vec{p}|$ . If  $p_\mu$  is small the dispersion relation in Eq. 3 can be expanded to

$$k = \omega \pm (p_0 - p \cos \theta) \quad (4)$$

Since plane polarization can be described as the superposition of two circularly polarized modes of opposite handedness, the lagging of one mode compared to the other as they propagate through space manifests as a rotation by some angle,  $\alpha$ , on the axis of the plane polarization

$$\alpha = \frac{1}{2}L(p \cos \theta - p_0) \quad (5)$$

Which, in turn, can be rewritten in terms of redshift,  $z$  and today's Hubble constant,  $H_0$ :

$$\alpha = \frac{p \cos \theta - p_0}{3H_0} \left[ 1 - (1 + z)^{-3/2} \right] \quad (6)$$

Unlike Faraday rotation, this rotation affects all photons at all frequencies equally, resulting in a uniform polarization rotation of light from any given emitter. Naturally, this rotation becomes much more prominent as light travels over larger distances and, as such, evidence for such rotation has been sought in the emission from distant galaxies and beyond to the CMB where signals of this effect would be strongest.

### 1.2. Impact of Cosmic Birefringence on CMB Power Spectra

The anisotropy of the CMB is often represented in the form of temperature ( $T$ ) and polarization ( $Q, U$ ) maps. It is useful to decompose the maps into scalar and  $\pm 2$  spherical harmonics for  $T$  and  $Q, U$  maps respectively (Zaldarriaga & Seljak 1997)

$$\begin{aligned} T(\hat{n}) &= \sum_{\ell,m} a_{\ell m}^T Y_{\ell m}(\hat{n}) \\ (Q \pm iU)(\hat{n}) &= \sum_{\ell,m} a_{\pm 2, \ell m} \pm 2 Y_{\ell m}(\hat{n}) \end{aligned} \quad (7)$$

and then convert the polarization maps into a basis of curl-free and divergence-free modes (colloquially known as  $E$ -modes and  $B$ -modes) using

$$a_{\pm 2, \ell m} = a_{\pm 2, \ell m}^E \pm ia_{\pm 2, \ell m}^B \quad (8)$$

Describing CMB maps in this way is often useful because any scattering of electrons due to propagating gravitational waves produces both E- and B-modes and thus is separable from other early-universe phenomena that source only Temperature and E-modes. The statistical properties of CMB polarization can then be described by the power spectra

$$C_\ell^{ij} = \frac{1}{2\ell + 1} \sum_m \langle a_{\ell m}^{i*} a_{\ell m}^j \rangle \quad (9)$$

Because E- and B-modes are pure-parity states, the correlation between B-modes and E-modes ( $C_\ell^{EB}$ ), and B-modes and T-modes ( $C_\ell^{TB}$ ) are zero by construction. In a scenario where the polarization of the CMB is rotated, however, some power leaks between  $E$ -modes and  $B$ -modes which results in non-zero power in  $EB$  and  $TB$  cross-correlation spectra as described by (Keating et al. 2013) and outlined below:

For a CMB polarimeter that measures Stokes  $Q$  and  $U$ , an offset in polarization rotation of  $\Delta\psi$  from the expected orientation results in the rotation of primordial  $\tilde{Q}$  and  $\tilde{U}$

$$Q \pm iU = e^{\pm 2i\Delta\psi} (\tilde{Q} \pm i\tilde{U}) \quad (10)$$

Where the tilde delineates the primordial values. From Eq. 10, the leakage between  $\tilde{Q}$  and  $\tilde{U}$  propagates into leakage from primordial  $E$ -modes to  $B$ -modes and vice versa

$$\begin{aligned} E &= \cos(2\Delta\psi)\tilde{E} + \sin(2\Delta\psi)\tilde{B} \\ B &= -\sin(2\Delta\psi)\tilde{E} + \cos(2\Delta\psi)\tilde{B} \end{aligned} \quad (11)$$

This in turn manifests as non-zero values measured in  $EB$  cross-spectra and also  $TB$  cross-spectra, since  $E$ -modes are correlated with  $T$ -modes as shown in Fig 1.

$$\begin{aligned} C_\ell^{TE} &= \cos(2\Delta\psi)\tilde{C}_\ell^{TE} \\ C_\ell^{EE} &= \sin^2(2\Delta\psi)\tilde{C}_\ell^{BB} + \cos^2(2\Delta\psi)\tilde{C}_\ell^{EE} \\ C_\ell^{BB} &= \cos^2(2\Delta\psi)\tilde{C}_\ell^{BB} + \sin^2(2\Delta\psi)\tilde{C}_\ell^{EE} \\ C_\ell^{TB} &= -\sin(2\Delta\psi)\tilde{C}_\ell^{TE} \\ C_\ell^{EB} &= \frac{1}{2}\sin(4\Delta\psi)\left(\tilde{C}_\ell^{BB} - \tilde{C}_\ell^{EE}\right) \end{aligned} \quad (12)$$

The origin of  $\Delta\psi$  is degenerate in that it could be due to some internal effect such as miscalibration of an experiment's co-polar axes (dubbed  $\bar{\phi}_Q$  in this report), or to some external effect such as cosmic birefringence ( $\alpha$  from Eq. 5), or a combination of the two.

$$\Delta\psi = \alpha + \bar{\phi}_Q \quad (13)$$

For an experiment interested only in measuring unbiased primordial  $B$ -modes, only the magnitude of the  $\Delta\psi$ , not the origin, is important. Since  $EB$  and  $TB$  correlations are canonically zero across all scales,  $\Delta\psi$  is estimated by fitting an angle to the cross spectra in Eq. 12 such that the power in  $C_\ell^{EB}$  and  $C_\ell^{TB}$  are minimized — a process referred in this report as EB/TB-minimization though it is often known as "self-calibration" in other texts.

While knowing the origin of polarization rotation is not essential for measuring  $B$ -modes, precisely measuring the instrumental polarization axis allows this degeneracy to be broken and enables such an experiment to probe for additional physical phenomena with data that already exists. Many

CMB experiments have published their attempts at measuring signals of cosmic birefringence, the results of which are shown in Table 1 which has been adapted from (Kaufman et al. 2016, Table 2). Currently, no significant Chern-Simons interactions have been detected via uniform polarization rotation measurements with upper-limits of only  $\alpha < \sim 1^\circ$ . Substituting  $H_0$  for  $h_0$ ,  $z$  for 1100, and solving for the mass in Eq. 6, this corresponds to  $p_0 - p \cos \theta \leq 1.1 \times 10^{-43} h_0 \text{ GeV}$ .

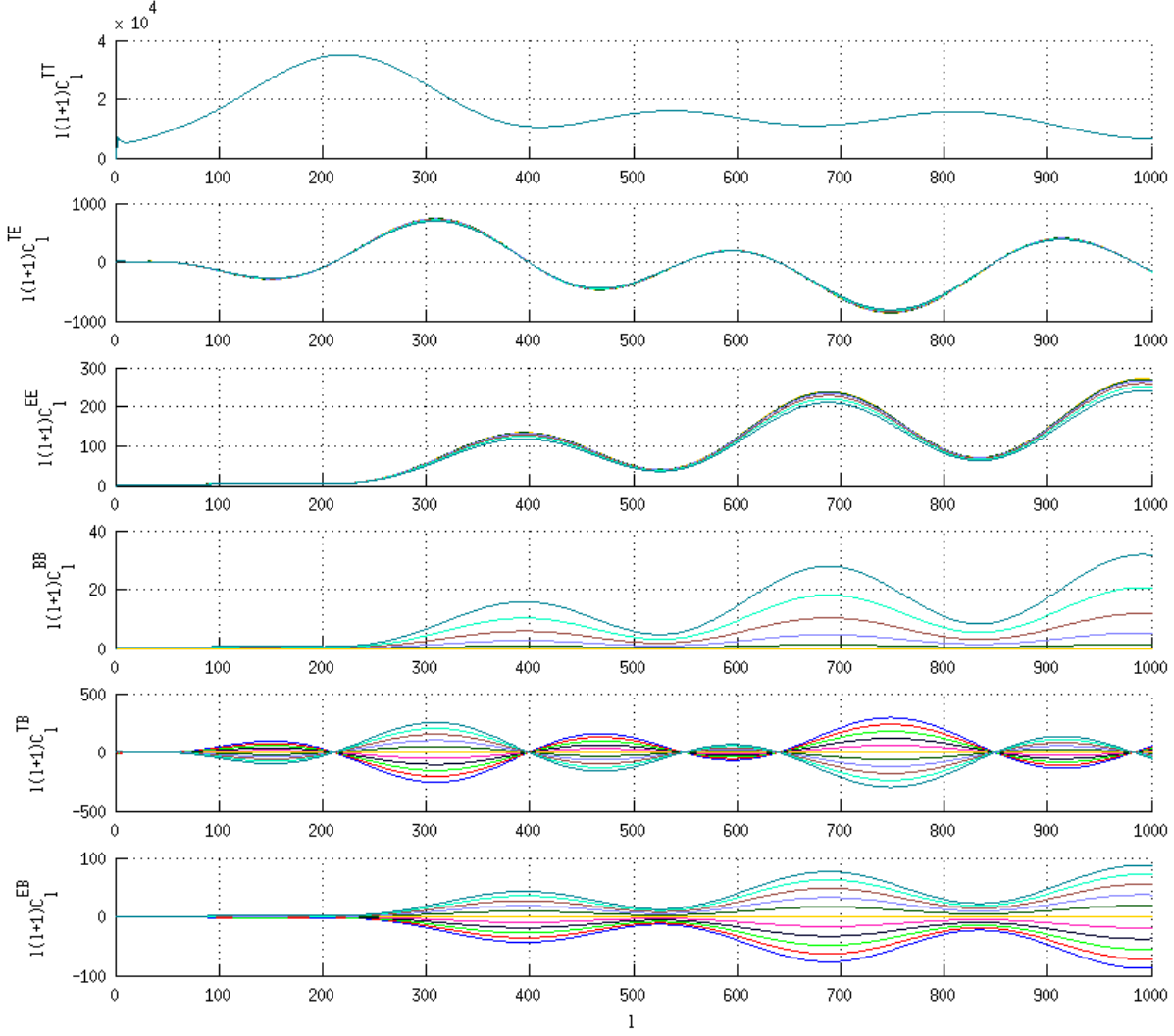


**Figure 1.**  $\Lambda\text{CDM}$  power spectra for rotations of polarization from  $-10^\circ$  (blue) to  $+10^\circ$  (teal)

Experiment	Frequency (GHz)	$\ell$ range	$\alpha(^{\circ})$	Calibration Method	Reference
QUaD	100	200-2000	$-1.89 \pm 2.24(\pm 0.5)$	polarized source	(Wu et al. 2009)
	150		$+0.83 \pm 0.94(\pm 0.5)$		
BOOM03	143	150-1000	$-4.3 \pm 4.1$	pre-flight polarized source	(Pagano et al. 2009)
ACTPol	146	500-2000	$-0.2 \pm 0.5(-1.2)$	"As-Designed"	(Finelli & Galaverni 2009)
WMAP7	41+61+94	2-800	$-1.1 \pm 1.4(\pm 1.5)$	pre-launch polarized source / Tau A	(Komatsu et al. 2011)
BICEP2	150	30-300	$-1 \pm 0.2(\pm 1.5)$	Dielectric Sheet	(Aiken 2013)
BICEP1	100+150	30-300	$-2.77 \pm 0.86(\pm 1.3)$	Dielectric Sheet	
			$-1.71 \pm 0.86(\pm 1.3)$	Polarized Source	(Kaufman et al. 2014)
			$-1.08 \pm 0.86(\pm 1.3)$	"As-designed"	
POLARBEAR	150	500-2100	$-1.08 \pm 0.2(\pm 0.5)$	Tau A	(Polarbear Collaboration et al. 2014)
<i>Planck</i>	30-353	100-1500	$0.35 \pm 0.05(\pm 0.28)$	pre-flight source / Tau A <sup>†</sup>	(Planck Collaboration et al. 2016a)

**Table 1.** Global Rotation Angle measurements and achieved precision for each notable CMB experiment.

<sup>†</sup> Calibration of polarization orientations were completed pre-flight in the near field and confirmed with celestial source Tau A within uncertainties (Rosset et al. 2010; Planck Collaboration et al. 2016b).

### 1.3. Precision Goal

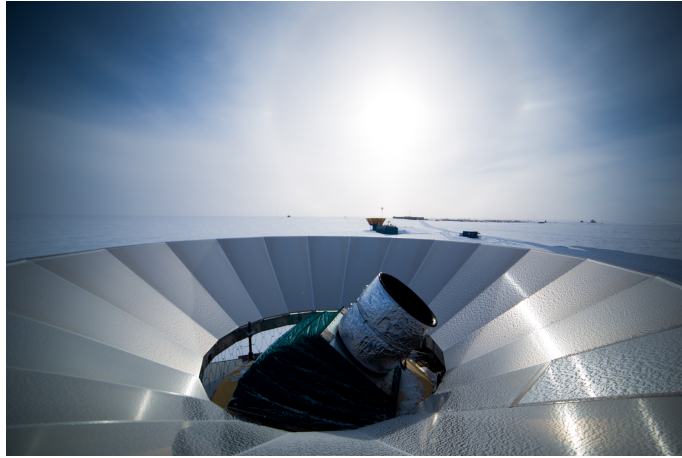
The statistical precision with which global polarization rotation is measured via EB/TB-minimization for contemporary BICEP/Keck experiments is  $O(0.1^{\circ})$  which is an order of magnitude smaller than the best external calibrations to-date<sup>1</sup>, predominantly due to systematic errors. Thus, the precision goal of this report is to meet or exceed an overall uncertainty of  $0.1^{\circ}$ .

### 1.4. The BICEP3 Polarimeter

The BICEP3 polarimeter is one of a family of experiments conducted by the BICEP Collaboration at the South Pole (Fig. 2). It is a 5.5 m-diameter aperture refracting telescope capable of finely measuring the fluctuations in temperature and polarization of the Cosmic Microwave Background at a frequency of 95 GHz (Ahmed et al. 2014). BICEP3 is capable of fielding up to 1280 pixels which consist of two co-located detectors that measure orthogonal polarizations so that each on-sky pixel is measuring both  $+Q$  and  $-Q$ . The pixels are grouped into 8px by 8px square tiles which can be removed and replaced without interfering with other tiles on the focal plane (Fig. 3). The telescope

<sup>1</sup> Internal data not yet published.

**Figure 2.** BICEP3 experiment completing test observations of the CMB circa Jan. 2016, courtesy BICEP Collaboration.



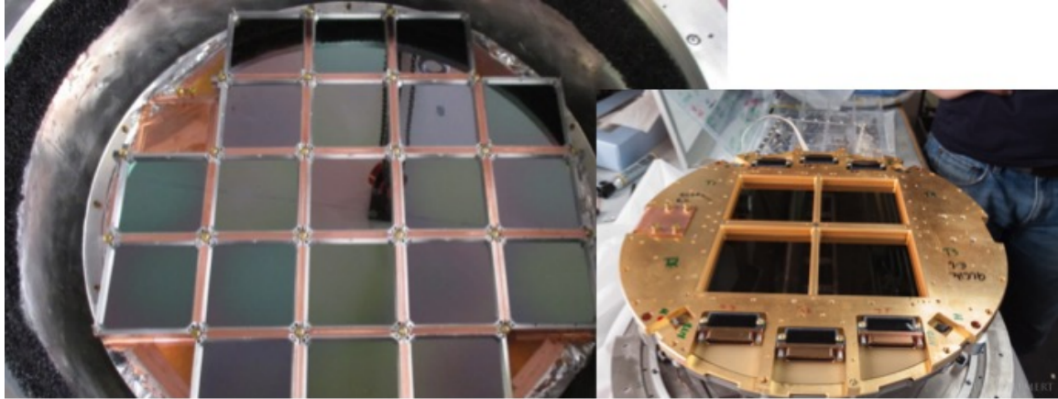
itself is mounted on a three-axis mount that moves in Azimuth and Elevation with an additional capability of rotating about the boresight axis, called Deck (*DK*).

The primary science goal of BICEP3 is to search for signatures of cosmic inflation which would manifest as B-mode polarization in the Cosmic Microwave Background (Ahmed et al. 2014). As shown in §1.2, if some sort rotation due to either a misestimation of the orientation of the instrument or cosmic birefringence exists, some E-modes will be rotated into B-modes resulting in some extra, unphysical B-mode signal. During CMB data analysis, any uniform rotation is accounted for using a EB/TB minimization method described in §1.2. To date, however, no external calibration of the co-polar axes of the BICEP3 detectors has been conducted. While this has no effect on its ability to accomplish its primary science goal, this leaves the instrument unable to distinguish the source of uniform angle offset if any is detected.

## 2. ROTATING POLARIZED SOURCE

In order to break the degeneracy between instrumental effects and cosmic birefringence, an independent measurement of BICEP3’s polarization orientation must be established by observing an external calibrator. In this case, a ground-based calibrator with well-characterized location, orientation, and polarization properties was used to complete this task.

**Figure 3.** **Left:** Fully populated BICEP3 focal plane with 20 tiles compared to the focal plane of its predecessor, Keck Array (**right**). Courtesy of (Hui et al. 2016).



To derive polarization polarization properties, we observe the RPS at different polarization rotations. The amplitude of the source as read out by a BICEP3 detector of an arbitrary polarization orientation should modulate as a function of RPS angle which, if modelled correctly, can be used to back-out polarization properties. Naturally, the statistical fluctuations and systematic offsets in both polarization angle and output of the source must be well controlled to ensure high precision in the calibration. This section describes the calibration equipment, addresses potential sources of systematic uncertainty, and describes the methodology with which observations of the RPS was conducted.

### 2.1. *Calibrator*

The Rotating Polarized Source (RPS) is a finely polarized, incoherent, electrically-chopped, broadband, noise source that is capable of  $> 360^\circ$  on-axis rotation. The RPS is comprised of four primary components: An electrically-chopped, broadband, thermal-noise source (BBNS), a polarizing wire grid, a precision rotation stage and a precision tilt meter (middle-right figure in Fig. 5).

The BBNS is a thermal source that can output up to 2 mW of power evenly over the W-band (75-110 GHz). The Johnson noise of a 50 Ohm resistor is amplified at 15GHz through a series of broadband power amplifiers which is then chopped via a PIN switch. The signal is then mixed to 95 GHz via a frequency multiplier, amplified by another power amplifier and then filtered with a W-band bandpass filter. The signal is then coupled to two adjustable attenuators to allow for amplitude

control before it is finally emitted via a 15dB rectangular feedhorn antenna. The stability of the source output is most sensitive to fluctuations in temperature and so is thermally controlled with internal heaters via PID feedback control.

Radiation from the source, upon leaving the feedhorn, is immediately coupled to a wire grid which further polarizes the light with < 0.05% emission in the cross-polar orientation (Bradford 2012). The wire grid is fixed to the source via a cylindrical shroud that is lined with Eccosorb HR-10 to absorb radiation that reflects off of the wire grid back toward the source.

The source and wire grid are then fixed to a ThorLabs NR360S precision rotation stage so that the polarization orientation of the source can be precisely controlled. The rotation stage is secured to an aluminum plate along with an Applied Geomechanics Model 801 uniaxial tiltmeter with < 0.001° repeatability<sup>2</sup> to monitor and control the absolute orientation of the source with respect to gravity.

The RPS is protected from the harsh Antarctic environment with an aluminum honeycomb enclosure. The inside of the enclosure is lined with Eccosorb HR-10 to mitigate RF reflections. The RPS emits out of a hole cut into the enclosure that is slightly oversized to prevent possible diffractions on the edges of the hole. To rule out any possible birefringent effects, no material was used to cover the hole in the enclosure. While this option made the RPS more susceptible to influence from the environment, maintaining the stability of source turned out to be quite feasible.

## 2.2. Nutation Angle Offset

If the feedhorn is not perfectly aligned along the axis of rotation of the rotation stage (i.e. has a non-zero nutation angle offset) the coupling coefficient between the RPS and a detector will have a 360° dependence. Since both the RPS and detector are polarized, the  $2\theta$  dependence of the resulting amplitude would have an additional  $1\theta$  dependence superimposed on top of it. This phenomena is discussed further in §3.7.2.

To mitigate issues from nutation offsets, the RPS feedhorn is fixed in place with an waveguide collar that can be oriented by three adjustable turnbuckles. The RPS is aligned by adjusting the

<sup>2</sup> According to manufacturer specifications.

turnbuckles such that, as the RPS rotates over  $360^\circ$ , the difference in amplitude between the peaks of the modulation curves when a detector is aligned in the E- and H-planes are minimized. The peak-differences for axially offset detectors were reduced to  $\sim 1\%$  and on-axis peak-differences were undetectable to  $< 0.1\%$ .

While high-precision alignment has been achievable, previous calibration campaigns ran into an issue with maintaining zero-nutation throughout assembly and deployment of the RPS in cold temperatures. After completion of the alignment procedure, the turnbuckles are held in place using locking nuts. To test the robustness of the alignment hardware, the RPS was assembled and placed outside on the MAPO roof multiple times to allow for thermal cycling and the alignment was re-measured each time. Despite multiple mock-deployments onto the MAPO roof, no detectable loss of alignment was measured.

### 2.3. *Polarization Stability*

The NR360S rotation stage has been thoroughly tested in-lab and the positional repeatability during bench tests has been shown to be better than  $0.01^\circ$  (Bradford 2012). During observations, the RPS is fixed atop a 12.5 m mast on the roof of the Martin A. Pomerantz Observatory (MAPO). Steel guy lines are used to secure the mast in place and level the RPS in the axis of rotation with respect to gravity (leftmost figure in Fig. 5). After leveling, the guy lines are tightened and secure the mast in place such that fluctuations in the level as read by the tilt meter varied by  $< 0.008^\circ$  during observations.

### 2.4. *Output Stability*

Detector polarization angles are calibrated by examining how the apparent amplitude of the source as seen by the detector modulates as a function of the orientation of the source's co-polar axis. As such, fluctuations in the source output would lead to a decrease in repeatability when estimating a detector's polarization angle. The gain of the power amplifiers in the BBNS are highly sensitive to fluctuations in temperature and initially the amplitude of the source, despite PID feedback control, could vary on the order of 20% or more throughout the day in the harsh and unpredictable Antarc-

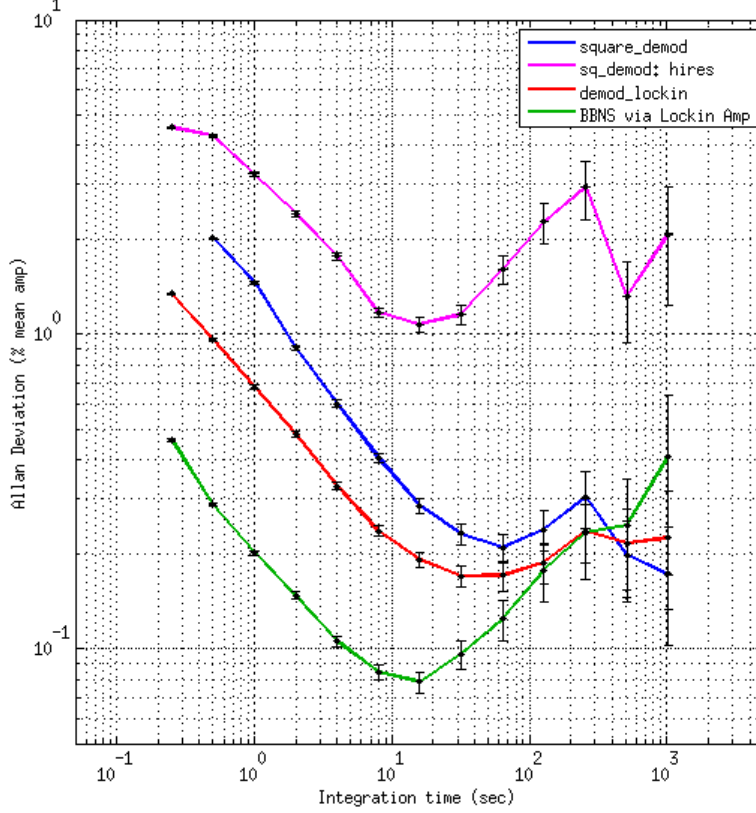


**Figure 4.** Plot of Allan deviation as a function of integration interval. The green line is a timestream recorded with the RPS placed atop the MAPO building and demodulated via SR830 Lock-In Amplifier. The other three lines represent a single timestream as read-out by a single detector on BICEP3 but digitally demodulated using three different functional approaches

tic weather. The thermal contact was improved between the source’s power amplifiers to the solid aluminum chassis to which all of the RF components are fixed, to reduce fluctuations in source amplitude. To quantify the output stability in Antarctic temperatures, the RPS output was monitored under two different scenarios. First, the RPS was placed on the rooftop of MAPO and coupled to a WR-10 detector diode which was read out by a SR830 Lock-In Amplifier the timestream of which was recorded via a LabJack U6 DAQ device. Whilst on the rooftop, a one-hour timestream was recorded with the RPS unmoving at a fixed command angle of  $0^\circ$ . Then, when the RPS was deployed on the calibration mast and another stability test was run where a single channel from BICEP3 centered on and observed the RPS for over an hour.

Figure 4 shows a comparison of Allan deviations as a function of integration time between the rooftop and on-mast stability measurements as demodulated by an SR830 Lock-In Amplifier and a three difference digital demodulation functions respectively. Under temperature control, the power fluctuations of the RPS as observed by BICEP3 with digital demodulation were marginally higher than the rooftop test ranging from 0.2% to 0.3% mean amplitude on timescales relevant to individual rasters ( $\sim 150\text{s}$ ). Though fluctuations on timescales relevant to whole rastersets ( $\sim 2000\text{s}$ ) aren't as well constrained, they are definitively  $< 0.5\%$  as observed by BICEP3.

To characterize the dependence of output power on command angle, the RPS and run through a mock observation schedule while deployed on the MAPO mast where it would rotate between  $-180^\circ$  to  $180^\circ$  in  $30^\circ$  increments, resting for five minutes between rotations. It was found in that fluctuations in source output were  $< 0.5\%$  of the mean amplitude with no detectable dependence of the source output on rotation angle.

### 2.5. *Polarization Calibration*

Knowledge of the co-polar axis of the RPS with respect to zenith is essential in order to back out the polarization orientation of detectors. The orientation of the polarizing wire grid is precisely measured with respect to the rotation stage. The rotation stage, with shroud and wire grid installed, was mounted onto a knee mill with wires of the grid (roughly) aligned to the  $x$ -axis of the knee mill's linear stage. The rotation stage was squared with a dial indicator such that the runout on both the  $x$ - and  $y$ -axis was much less than  $25\,\mu\text{m}$  over  $150\,\text{mm}$  in both directions. A centering scope was installed into the knee mill and the rotation stage was commanded to an angle such that the travel of the wires as viewed from the centering scope while moving the rotation stage along the mill's  $x$ -axis was less than the width of the single wire ( $15\,\mu\text{m}$ ) over the length of the aperture of the shroud ( $80\,\text{mm}$ ). The polarizing grid was measured to be  $+2.50^\circ \pm 0.01^\circ$  offset from zero.

### 2.6. *Pointing*

As will be discussed further in §3.7.2, systematic effects can arise due to projection effects if the RPS is not pointing directly at the telescope. Two red tags are secured to the back of the RPS such

**Figure 5.** Example images of the typical RPS calibration campaign. **Leftmost:** RPS deployed atop a calibration mast, secured by guy-lines. **Middle-left:** BICEP3 with calibration mirror installed. **Middle-right:** RPS benchtop setup - broadband noise source with absorptive shroud and wire grid secured to precision rotation stage. **Rightmost:** Zoomed image of RPS installed in environmental enclosure shows alignment strips. Images courtesy of the BICEP Collaboration.



that if both tags can be seen evenly from the telescope aperture, the RPS is pointing directly toward the telescope to within  $< 1^\circ$  in Azimuth (Rightmost figure in Fig. 5). The pointing of the RPS in the Elevation was not well constrained during the observations beyond ensuring that the mast was secured such that fluctuations due to rocking were established to be  $< 0.008^\circ$  during observations.

## 2.7. *Observations*

The polarization properties of each detector on BICEP3 are characterized by mapping their spatial response via observations of the RPS over a two-week long calibration campaign. Because the RPS was located on the sky well below the operational elevation of the instrument, a large, flat aluminum mirror was installed over the telescope to redirect the beams onto the horizon (middle-left figure in Fig. 5).

Observations of the RPS were made in 5-minute long rasters of  $9^\circ$  Azimuth by  $2^\circ$  Elevation in  $0.1^\circ$  steps of Elevation in order to map beams of the detectors in a given section of the focal plane (Figure 10). During each raster, the RPS commanded to a polarization angle and remained fixed until the raster completed. A set of 13 rasters, dubbed a rasterset, were recorded over the same Az/El region as the RPS rotated through a full  $360^\circ$  in  $30^\circ$  steps. This ensured that, for detectors in a given section of the focal plane, full beam maps were measured over a full  $360^\circ$  of linear polarization.

Coverage of the entire focal plane was divided into 3 observing schedules, each consisting of 19 rastersets and taking 13.5 hours to complete. The telescope was expected to be capable of observing for 48 consecutive hours before sub-kelvin helium-sorption cooler needed to be cycled, so two schedules were run back-to-back, minimizing the number of fridge cycles required to complete total focal plane coverage. A total of 57 rastersets with different Azimuth and Elevation offsets are completed to ensure that all detectors across the focal plane have full beam maps across  $360^\circ$  of RPS rotation at a single DK-angle. The RPS observation campaign, conducted mid-January of 2018, consisted of measurements covering all channels of the focal plane at DK-angles of  $1.25^\circ$ ,  $46.25^\circ$ ,  $91.25^\circ$ , and  $135.25^\circ$  with an additional measurement of two-thirds of the focal plane covered again at a DK-angle of  $46.25^\circ$ . The extra  $0.25^\circ$  offset was to account for a known offset in DK-angle due to the way the telescope is physically installed in the mount which is not accounted for in the pointing model. All five measurement sets total to  $\sim 3500$  rasters or 12 consecutive observing days.

### 2.8. Data Acquisition

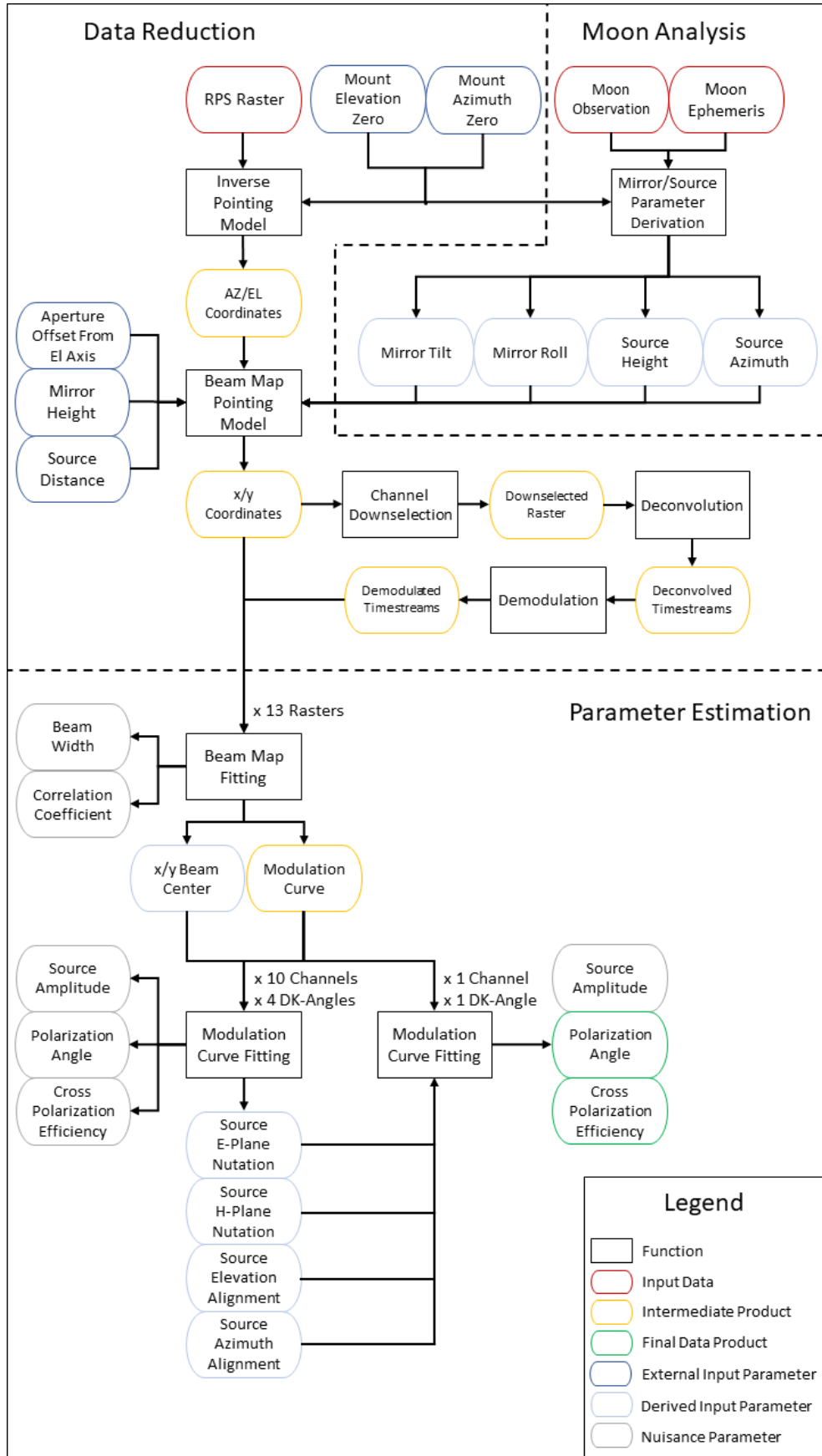
The raw data of RPS observations comes in the form of timestreams of all quantities measured by the telescope control system which includes detector amplitudes and raw mount encoder information and is well described in (BICEP2 Collaboration et al. 2014a). The square-wave reference signal used to chop the RPS is fed into an auxiliary readout port on the telescope control hardware so that the chop reference is packaged alongside the data for easy demodulation during the data reduction process described in §3.3.

## 3. ANALYSIS

This section describes the approach taken to extract per-pixel polarization properties from raw per-channel timestream data of RPS observations. A simplified flowchart of the analysis approach is shown in Fig. 6.

In summary, a timestream for each detector is reduced to produce unbinned beam maps in AZ/EL-space for a given DK-angle. Beam maps are converted from topocentric horizon coordinates ( $Az$ ,  $El$ ,  $DK$ ) to more useful focal plane "co-moving" coordinates ( $x$ ,  $y$ ,  $\phi$ ) via a beam map

**Figure 6.** Simplified flowchart of RPS observation analysis where per-pixel polarization properties are extracted from raw timestream data of observations of the RPS.



pointing model. Rasters are concatenated together and a 2-D Gaussian beam profile is fit across a whole rasterset of beam maps which produces a modulation curve as a function of RPS rotation angle. A modulation curve model is then fit to the beam map-derived amplitudes to estimate the polarization angle and cross-polar efficiency of each channel. Polarization angles of both channels per pixel are combined into a single response angle of from BICEP3's assumed  $Q$ -axis. Finally, the uniform rotation angle,  $\bar{\phi}_Q$ , is estimated based on the contribution of each pixel to BICEP3 CMB maps across a whole CMB observing season.

### 3.1. *Polarized Beam Map Pointing Model*

During analyses dealing with beam data, it is useful to work within a coordinate system that is defined in the reference frame of the focal plane. This section describes the process of converting topocentric horizon coordinates of ( $Az$ ,  $El$ ,  $DK$ ) into a co-moving coordinate system that is referenced to the telescope boresight via what is called the Beam Map Pointing Model.

The direction in which the telescope boresight is pointing in the timestream data is given in the form of raw encoder values. During the data reduction process, an inverse pointing model converts raw encoder values to topocentric horizon coordinates ( $Az$ ,  $El$ ) with an extra orientation coordinate DK (pronounced Deck) using Azimuth- and Elevation-zero offset parameters derived from optical star pointing.

Then, for a given source on the sky, the Beam Map Pointing Model returns the location and orientation of the source as it would appear over the focal plane in  $(x, y, \phi)$  coordinates using various mount, mirror, and source parameters as inputs.

We start by defining a Cartesian coordinate system with its origin defined as a point on the telescope Azimuth axis at the height of the telescope groundshield. The  $x$ -axis points in the  $Az=0^\circ$  direction and the  $z$ -axis points toward zenith. The  $y$ -axis is defined as

$$\hat{y} = \hat{z} \times \hat{x} \quad (14)$$

and points along the  $Az=-90^\circ$  axis.

An orthonormal basis,  $\hat{B}$ , is defined to represent the pointing and orientation of the telescope boresight where  $\hat{B}_3$  is the telescope pointing and  $\hat{B}_1$  is the orientation axis and  $\hat{B}_2$  is defined in the right-handed sense (i.e.  $\hat{B}_2 = \hat{B}_3 \times \hat{B}_1$ ).  $\hat{B}_3$  is initialized pointing along the  $z$ -axis and  $\hat{B}_1$  is initialized pointing along the  $x$ -axis.

$$\hat{B}_3 = \begin{bmatrix} 0 \\ 0 \\ 1 \end{bmatrix}, \hat{B}_1 = \begin{bmatrix} 1 \\ 0 \\ 0 \end{bmatrix} \quad (15)$$

These vectors are put through a series of rotations using an Euler rotation matrix of the form

$$\mathbf{M}(\alpha, \beta, \gamma) = \begin{bmatrix} \cos \alpha \cos \beta \cos \gamma - \sin \alpha \sin \gamma & -\cos \alpha \cos \beta \sin \gamma - \sin \alpha \cos \gamma & \cos \alpha \sin \beta \\ \sin \alpha \cos \beta \cos \gamma + \cos \alpha \sin \gamma & -\sin \alpha \cos \beta \sin \gamma + \cos \alpha \cos \gamma & \sin \alpha \sin \beta \\ -\sin \beta \cos \gamma & \sin \beta \sin \gamma & \cos \beta \end{bmatrix} \quad (16)$$

Where the vectors are rotated by  $\gamma$  about the  $z$ -axis, then by  $\beta$  about the  $y$ -axis, then about  $\alpha$  about the  $z-axis$ .  $\hat{B}_1$  and  $\hat{B}_3$  are rotated first about Deck, then Elevation and finally Azimuth:

$$\mathbf{M}(-AZ, 90^\circ - EL, DK - 90^\circ) \hat{B}_i \quad (17)$$

An additional vector,  $\vec{A}$ , representing the telescope aperture position is defined at the origin.

$$\vec{A} = \begin{bmatrix} 0 \\ 0 \\ 0 \end{bmatrix} \quad (18)$$

$\vec{A}$  is similarly rotated but has an additional translation to reflect the actual position of the aperture in 3-Dimensional space:

1. Rotate by DK:  $M(0, 0, DK - 90^\circ) \vec{A}$
2. Translate in the  $z$ -direction by the distance to the aperture from the EL axis:  $\vec{A} + (0, 0, d_{EL \rightarrow A})$

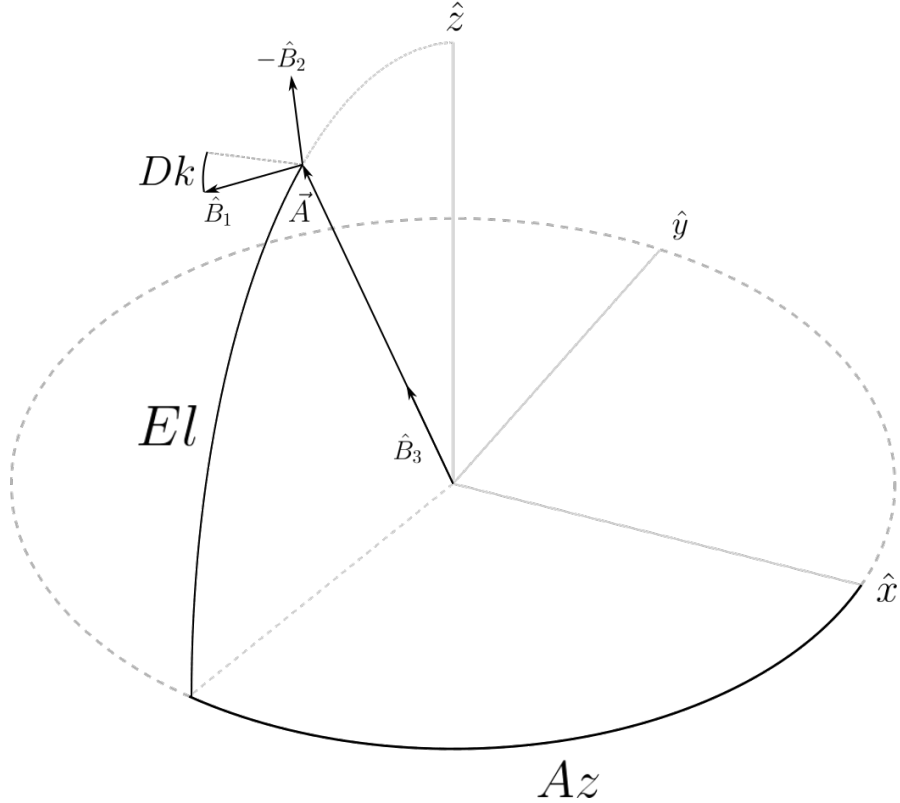


**Figure 7.** Diagram showing the relationship between topocentric horizon coordinates and pointing, orientation, and aperture position vectors.

3. Rotate by EL and AZ:  $M(-AZ, 90^\circ - EL, 0)\vec{A}$

The basis vectors  $\hat{B}_1$ ,  $\hat{B}_2$ , and  $\hat{B}_3$  along with the aperture position fully describe the pointing, orientation and location of the telescope in Cartesian space, a diagram of which is shown in Figure 7.

The direction in which a detector is sensitive, called the detector pointing, is represented as some angular offset with respect to the boresight pointing. For a detector sensitive to some arbitrary direction given in the form of the pointing vector  $\hat{D}_3$ , boresight-centered coordinates  $r$  and  $\theta$  are defined where  $r$  is the projection angle of  $\hat{D}_3$  on  $\hat{B}_3$  and  $\theta$  is the bearing angle from the  $\hat{B}_1$ -axis to

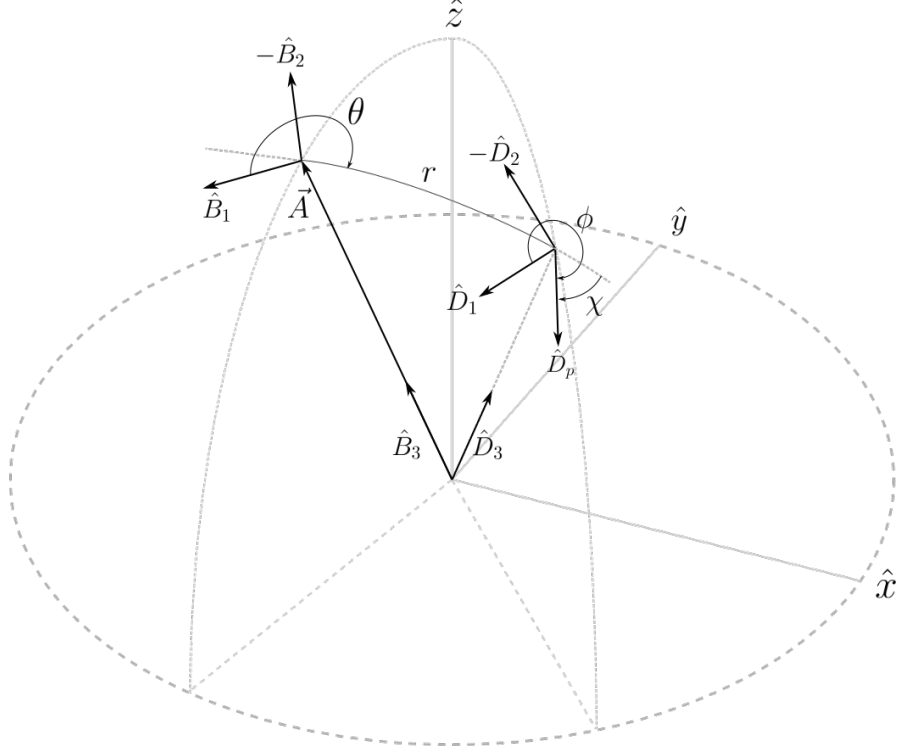


**Figure 8.** Diagram showing the relationship between boresight vectors, detector vectors, and conversion to co-moving coordinates.

the great circle connecting  $\hat{B}_3$  to  $\hat{D}_3$  (Fig. 8). The positive  $\theta$  direction is measured from  $\hat{B}_1$  toward  $-\hat{B}_2$  in keeping with collaboration-wide convention.

$$\begin{aligned} r &= \cos^{-1} \left( \hat{D}_3 \cdot \hat{B}_3 \right) \\ \theta &= \tan^{-1} \left( \frac{-\hat{D}_3 \cdot \hat{B}_2}{\hat{D}_3 \cdot \hat{B}_1} \right) \end{aligned} \quad (19)$$

In the case of beam mapping, it is often useful to represent pointings in a rectangular coordinate system which is converted from  $r$ - $\theta$  coordinates to  $x$ - $y$  rectangular coordinates using Lambert azimuthal equal-area projection:

$$\begin{aligned} x &= 2 \sin r / 2 \cos \theta \\ y &= 2 \sin r / 2 \sin \theta \end{aligned} \quad (20)$$

Lambert projection is used as a standard across all BICEP calibration analyses and is particularly useful during Far Sidelobe Mapping where data is very far away from the boresight.

For completeness, another coordinate describing the co-polar orientation of an object with respect to the boresight orientation is needed. An angle  $\phi$  is defined as an angle measuring an orientation direction, in the tangent plane at any  $x,y$  point, relative to the local orientation vectors. For a detector with a co-polar axis described by  $\hat{D}_p$ , the  $\phi$ -angle, denoted as  $\phi_d$  for detectors, is measured from the  $\hat{D}_1$ -axis, *away* the  $\hat{D}_2$ -axis:

$$\hat{D}_p = \hat{D}_1 \cos \phi - \hat{D}_2 \sin \phi \quad (21)$$

Where the local orientation vectors  $\hat{D}_1$  and  $\hat{D}_2$  are the parallel transports of  $\hat{B}_1$  and  $\hat{B}_2$  along the great circle connecting the boresight pointing to an arbitrary  $x$ - $y$  point:

$$\begin{bmatrix} \hat{D}_1 \\ \hat{D}_2 \\ \hat{D}_3 \end{bmatrix} = \begin{bmatrix} \cos r \cos^2 \theta + \sin^2 \theta & (1 - \cos r) \cos \theta \sin \theta & -\sin r \cos \theta \\ (1 - \cos r) \cos r \sin \theta & \cos r \sin^2 \theta + \cos^2 \theta & \sin r \sin \theta \\ \sin r \cos \theta & -\sin r \sin \theta & \cos r \end{bmatrix} \begin{bmatrix} \hat{B}_1 \\ \hat{B}_2 \\ \hat{B}_3 \end{bmatrix} \quad (22)$$

Similarly, the direction of an on-sky source can also be represented in coordinates with respect to the boresight. For a point-like source at some Azimuth on the sky  $AZ$ , height above the origin  $d_h$ , and at a distance  $d_S$  the source position,  $\vec{S}$ , in Cartesian space is

$$\vec{S} = \begin{bmatrix} d_S \cos AZ \\ -d_S \sin AZ \\ d_h \end{bmatrix} \quad (23)$$

To account for parallax, the pointing vector of the source,  $\hat{S}_3$ , is the unit vector pointing from the aperture position to the source position:

$$\hat{S}_3 = \frac{\vec{S} - \vec{A}}{|\vec{S} - \vec{A}|} \quad (24)$$

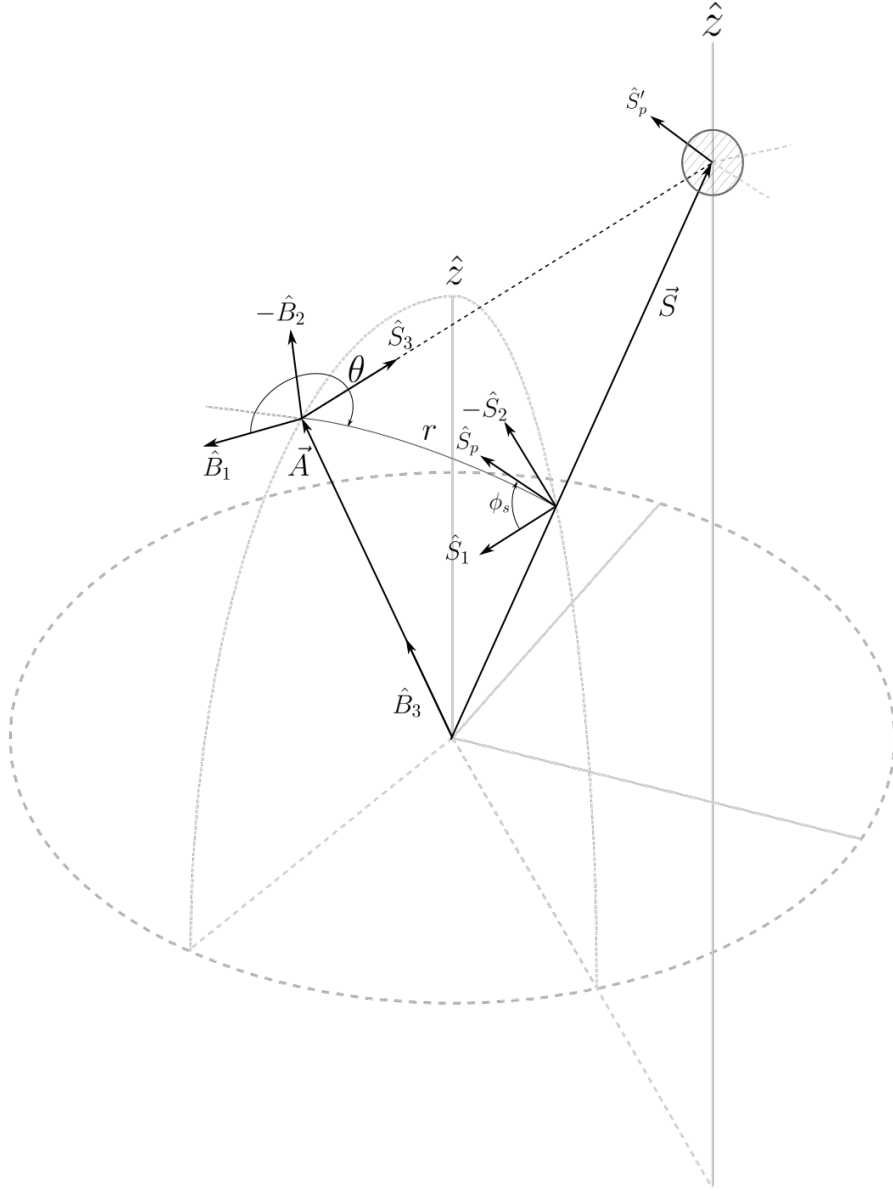


**Figure 9.** Diagram showing the relationship between boresight vectors, source vectors, and conversion to co-moving coordinates.

Which can then be converted into  $r\theta$  coordinates using Eq. 19 and then to  $x$ - $y$  coordinates via Eq. 20.

In the case of a polarized source, the apparent polarization orientation,  $\hat{S}_p$ , is the projection of the actual source polarization direction,  $\hat{S}'_p$ , onto the plane tangent to  $\hat{S}_3$  (Fig. 9).

$$\begin{aligned}\hat{S}_{p,2} &= \frac{\hat{S}'_p \times \hat{S}_3}{\left| \hat{S}'_p \times \hat{S}_3 \right|} \\ \hat{S}_p &= \hat{S}_3 \times \hat{S}_{p,2}\end{aligned}\quad (25)$$

The source  $\phi$ -angle,  $\phi_s$ , is then the angle measured from  $\hat{S}_1$  to  $\hat{S}_p$  away from  $\hat{S}_2$ .

$$\phi_s = \tan^{-1} \left( \frac{-\hat{S}_2 \cdot \hat{S}_p}{\hat{S}_1 \cdot \hat{S}_p} \right) \quad (26)$$

Thus, the pointing model fully describes the direction and polarization orientation for a given detector in coordinates that are referenced to telescope boresight. Likewise, for a polarized source on the sky, the pointing model fully describes its location and polarization orientation as it is projected onto the focal plane with respect to the telescope boresight when it is pointing and oriented in any given direction.

### 3.1.1. Mirror Reflections

Since it is unable to view objects at low Elevations during normal operation, the telescope uses a flat mirror to reflect rays onto the horizon. The mirror co-moves with the telescope and is allowed two axes of rotation, *Tilt* and *Roll*. Reflections from a flat mirror are computed in the pointing model by defining a vector normal the plane of the mirror where, for a mirror with zero *Tilt* and *Roll*, rays are reflected directly back toward the telescope (i.e.  $\hat{n} = -\hat{B}_3$ )

$$\hat{n} = \begin{bmatrix} 0 \\ 0 \\ -1 \end{bmatrix} \quad (27)$$

The orientation of the mirror with is calculated by rotating by *Roll* and *Tilt* and then rotating by Az and El:

1. Rotate by Roll:  $\mathbf{M}(90^\circ, \text{Roll}, 0)\hat{n}$
2. Rotate by Tilt:  $\mathbf{M}(0, \text{Tilt}, 0)\hat{n}$
3. Rotate by EL and AZ:  $\mathbf{M}(-\text{AZ}, 90^\circ - \text{EL}, 0)\hat{n}$

The pointing and orientation vectors are then reflected by

$$\begin{aligned}\hat{B}'_1 &= \hat{B}_1 - 2(\hat{B}_1 \cdot \hat{n})\hat{n} \\ \hat{B}'_3 &= \hat{B}_3 - 2(\hat{B}_3 \cdot \hat{n})\hat{n}\end{aligned}\tag{28}$$

The mirror flips parity, so the third unit vector is now constructed in the left-handed sense

$$\hat{B}'_2 = \hat{B}'_1 \times \hat{B}'_3\tag{29}$$

The apparent aperture position is computed by first determining the mirror position,  $\vec{A}_m$ , which is calculated the same way as  $\vec{A}$  but with an additional height from the aperture to the mirror added to the translation distance. The apparent aperture position is then calculated as

$$\vec{A}' = \vec{A} - 2((\vec{A} - \vec{A}_m) \cdot \hat{n})\hat{n}\tag{30}$$

Which is substituted for  $\vec{A}$  when determining the source pointing vector in Eq. 24.

### 3.2. Derivation of Mirror Orientation and Source Location

The *Tilt* and *Roll* parameters of the mirror are used in the beam map pointing model to calculate the reflection of rays and apparent aperture position. Because the location of the source as it is projected onto the focal plane affects the source's apparent polarization orientation, knowledge of the orientation of the calibration mirror to high precision is essential. It is possible to physically measure the tilt and roll of the mirror *in-situ*, but a higher precision measurement can be achieved by observing celestial bodies with well-characterized ephemerides such as the Moon. Mirror parameters are estimated by fitting a 2D Gaussian beam to beam maps from the moon and optimizing *Roll* and *Tilt* parameters in the beam map pointing model such that the residuals between Moon-derived

beam centers and beam centers derived from CMB observations (BICEP2 Collaboration et al. 2014b, §IV) (without the mirror) are minimized. The location of the Moon is known to great precision so uncertainty on the beam center estimations dominated the resulting repeatability on the mirror parameters, the impact of which is discussed further down in §3.11.

For the same reason that the mirror orientation must be characterized to a high precision, so too must the location of the RPS. After acquiring the mirror parameters, a similar method is used to estimate the location of the source. A Gaussian beam model is fit to beam maps from the RPS and the location of the source was chosen such that the residuals between RPS-derived beam centers and CMB-derived beam centers are minimized.

For the December 2017 to February 2018 calibration season, the data from which this report analyzes, no observations of the Moon were conducted due to insufficient time. The previous year however had both Moon and preliminary RPS observations. While the RPS data from January 2017 was not usable for the purpose of polarization calibration, the data was sufficient for deriving the location of the RPS for that season using method described above. For the 2017/2018 season, the same location for the source was used as input into the beam map pointing model under the assumption that the change in location of the RPS due to redeployment on the MAPO mast is repeatable on the order of  $0.1m$  in height and  $0.5m$  in any other direction, corresponding to  $0.15^\circ$  in Azimuth and  $0.03^\circ$  in Elevation. Since no Moon observations could be used, RPS observations were used instead to derived the mirror orientation since the source location was already known.

### 3.3. *Data Reduction*

Reduction of the data is performed on the raster level. The data directly from the telescope comes in the form of detector timestreams along with readout of the telescopes Azimuth, Elevation, and Deck encoders. The very first step in the reduction is to convert the encoder values into the actual pointing of the telescope boresight in AZ, EL, and DK through what is called the inverse pointing model. The model first converts the encoder values directly into an AZ, EL, and DK via some known conversion factor. Then the AZ and EL values are offset according to the known pointing

of the telescope derived from optical star pointing with an accuracy of  $0.8^\circ$  in Azimuth and  $0.1^\circ$  in Elevation. The  $DK$  rotation offset is accounted for *a priori* in the pointings of the detectors.

The raw data from the telescope for any given raster contains timestreams from all detectors across the focal plane. Only  $\sim 70$  of the 2640 detectors are actually covered in a given raster, so the reduction code uses detector pointings derived from CMB data (BICEP2 Collaboration et al. 2014b, §IV) to cut detector timestreams that are not sufficiently within the coverage area. Having a sufficient amount of the beam measured for a detector is essential during the beam-fitting process. If a detector beam center is right on the the coverage boundary, half of the beam is cut off which adds extra error during beam-fitting. As such detectors only pass cuts if their beam centers within the coverage area *and* at least a half beam-width ( $0.15^\circ$ ) away from the coverage boundary as shown in Fig 10.

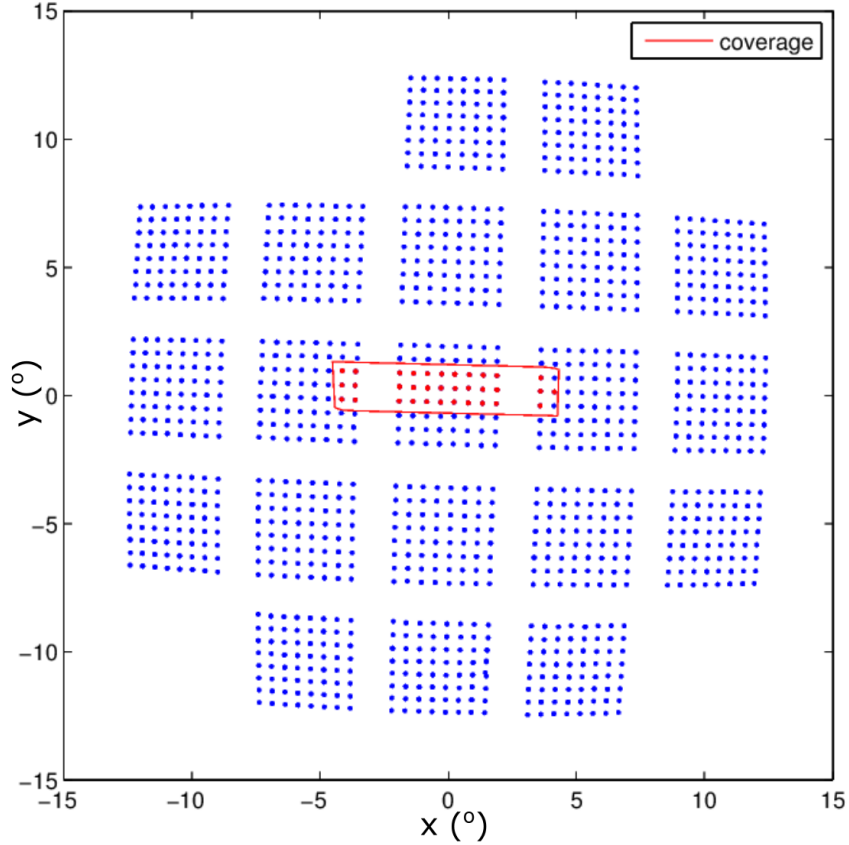
Downselection is completed by first converting topocentric horizon coordinates for the raster into boresight centered coordinates. A boundary is drawn around the boresight-centered coordinates to represent the coverage over the focal plane and all detectors outside of this boundary are cut from the dataset.

### 3.4. Timestream Deconvolution

After channel down-selection the timestreams are deconvolved from the temporal response of the instrument due to downsampling and low-pass filtering during on-site handling of the data. Measurements of the transfer functions of the telescope readout electronics and data handling systems were made separate from this analysis. The transfer functions were then multiplied together in frequency space and then inverted and Fourier Transformed into a deconvolution kernel. The deconvolution kernel was then convolved with individual detector timestreams to remove the effects of the readout and data handling processes. The deconvolution step also has the ability of including an arbitrary shift in the timestreams which enables for all of the demodulated signal to be isolated in the in-phase term in the demodulation step with sub-sample resolution.

### 3.5. Chop Demodulation

**Figure 10.** Plot of  $x$ - $y$  detector pointings (blue dots) with coverage boundary of an example raster (red line). Detectors considered to be sufficiently covered are marked in red.



The amplitude of the RPS was chopped via an RF PIN switch in the signal chain of the BBNS so that the signal from the RPS could be isolated from ambient sources in the data via demodulation. As part of the BICEP/Keck Collaboration pipeline, reduction of calibration data has historically used a square-wave demodulation routine called `square_demod`<sup>3</sup> which, in essence, identifies phases in individual chop cycles in a timestream and combines them to determine the in-phase signal. A fundamental issue with `square_demod` was that ambiguous phases in the chop reference were randomly assigned to either preceding or following it, rendering the demodulator non-deterministic which was unacceptable for the level of precision required in BICEP3 calibration projects. In an orthogonal calibration effort, `square_demod` was upgraded with a "High Resolution" option<sup>4</sup> which interpolated

<sup>3</sup> Developed by Dr. Walt Ogburn, Stanford University

<sup>4</sup> Developed by Mr. Tyler St. Germaine, Harvard University

the chop reference signal for more accurate chop cycle selection, both handling spurious steps and glitches in the data much better and also making the function deterministic as was required.

The "hi-res" upgrade to `demod_lockin`, however, appeared to fail at properly tracking the phase of the chop reference signal, resulting in steps in the data and leakages between in-phase and quadrature term timestreams which worsened over time. In response, I developed my own demodulation routine based on Lock-on amplification principles. Unlike the square-wave demodulator which handles the chop reference chop-cycle-by-chop-cycle, the lock-in demodulator treats the chop reference as a continuous function.

First, the sine wave at the chop frequency is isolated from the other harmonics that make up the square-wave reference signal using a band-pass filter. The width of the band-pass filter is chosen such that, in addition to the harmonics, the sidebands around the chop frequency due to quantization of the square wave are also filtered out.

Next, the filtered chop reference is mixed with the timestream which, in terms of frequency, shifts the signal from the RPS into a DC-component and a component at a frequency that is twice the chop frequency. The high-frequency component is discarded using a low-pass filter, leaving only the isolated RPS signal. Great care was taken in choosing the width of the low-pass filter as too wide of a filter would leave a noisy signal and too narrow would begin to remove real features in the data, affecting the shape of the beam in the timestreams. The plots in Figure 11 show a timestream in which a small group of detectors on the telescope were centered on the RPS and observed unmoving for 1.5 hours. The timestream was demodulated using both demodulators and a side-by-side comparison is shown.

The demodulator has excellent background rejection capabilities such that the noise floor of demodulated timestreams are typically  $\sim 0.05\%$  of the peak amplitude compared to  $\sim 6\%$  in the square-wave demodulator. Figure 12 shows an extended beam map for a single pixel with the different demodulators applied to it. The first raster from every rasterset in a 13-hour schedule was demodulated using the various demodulators and concatenated to form an extended beam map binned in  $1^\circ$  pixels and spanning  $13^\circ$  in Azimuth and  $\sim 30^\circ$  in Elevation centered on the RPS. Sharp features which can be

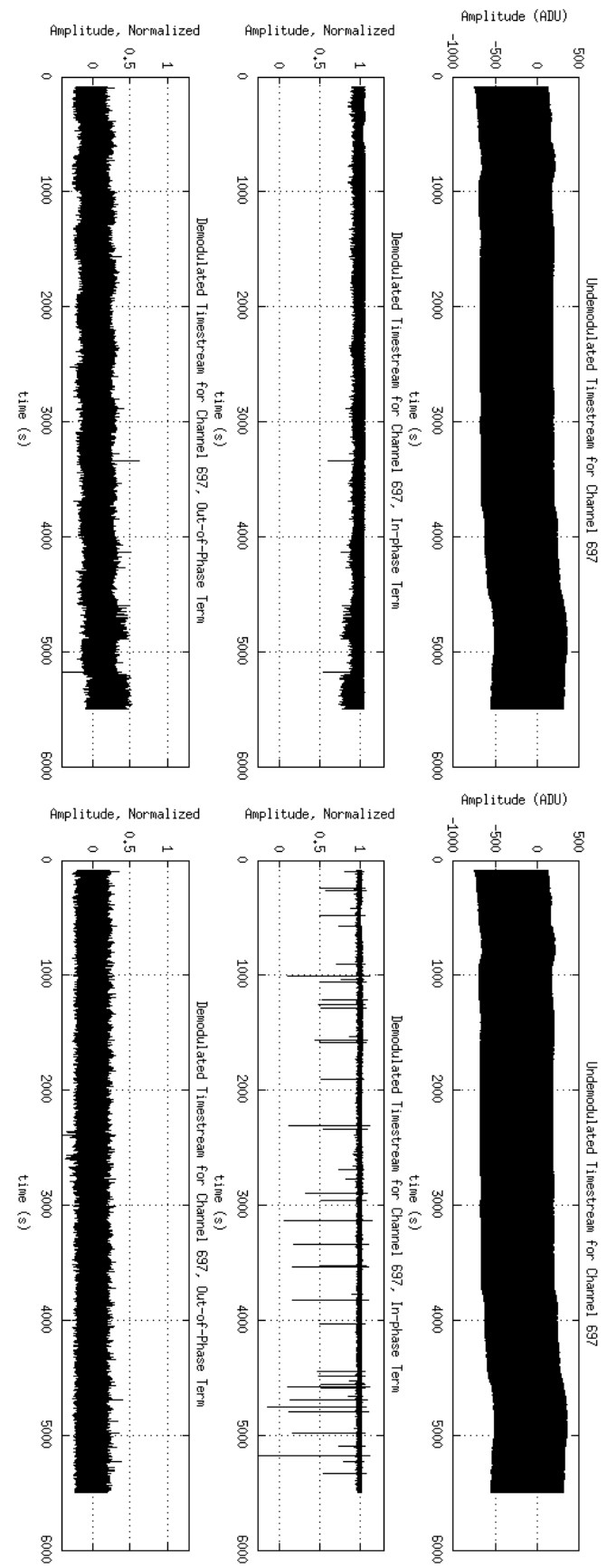


**Figure 11.** Side-by-side comparison of a 1.5-hour demodulated timestreams for a single detector. The **top** plot shows the undemodulated timestream, the **middle** shows the in-phase term of the post-demodulation timestream, and the **bottom** plot shows the out-of-phase term. On the left, the results of the square-wave demodulator are shown with increased noise (compared to the lock-in) and leakage between in-phase and quadrature terms that increases in severity over time. The right shows the lock-in demodulator that has a higher signal-to-noise, though spurious spikes as a result of dropped data frames in the on-site data-handling electronics are more prevalent in the these timestreams.

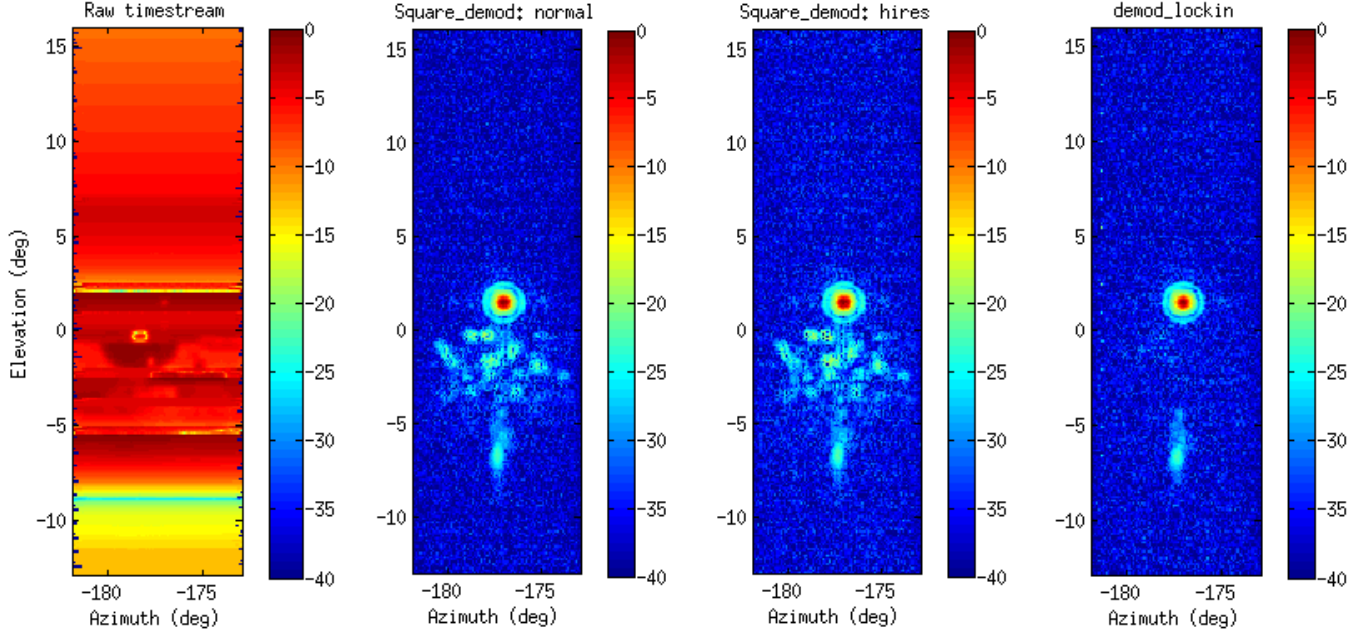


**Figure 12.** Extended beam map for a single well-behaved detector pre- and post-demodulation. Structure present in all post-demodulation maps at  $\sim -7^\circ$  is reflections of light from the RPS off of the ground.

seen in the raw timestreams leak into the signal from both `square_demod` functions while almost all background signals are rejected in the lock-in demodulator leaving only the RPS and ground-reflected signal.

In raster data which last only  $\sim 5$  minutes, spurious spikes in the data are relatively rare ( $< 1$  per raster on average) and because the beam of a detector is small compared to the area covered in a raster, their impact on parameter estimations was negligible. That said, data timestreams were ultimately demodulated using a digital lock-in demodulation procedure. Both demodulators have their merits however. While the Lock-in demodulator possesses superior background rejection it currently is not capable of handling spurious glitches or steps in the timestreams due to data handling errors. At some point in the future, it is planned to combine the best parts of both demodulators into a single function that is standard across calibration efforts.

### 3.6. Batch Reduction

As mentioned in §2.7,  $\sim 3500$  rasters must be individually reduced. Reduction on such a large scale was not feasible on a single machine, so the reduction pipeline includes a feature which delegates or "farms" reduction of individual rasters simultaneously across multiple machines on *Odyssey*, greatly reducing the time required to complete data reduction.

### 3.7. Parameter Estimation Strategy

Parameter estimation is performed using  $\chi^2$ -minimization via a MATLAB wrapper of the *MINUIT* function minimization routine (James & Goossens 1998). Parameter estimation is divided into two primary parts, beam parameter estimation of beam maps for each raster set, and then polarization parameter estimation for all raster sets of a given channel.

#### 3.7.1. Gaussian Beam Model

For each detector, A 2D Gaussian profile of the form

$$A_{B,i}(x, y) = A_{0,i} \exp \left[ -0.5 \left[ (x - x_0)^2 \Sigma_{11}^{-1} + (y - y_0)^2 \Sigma_{22}^{-1} + 2(x - x_0)(y - y_0) \Sigma_{21}^{-1} \right] \right] \quad (31)$$

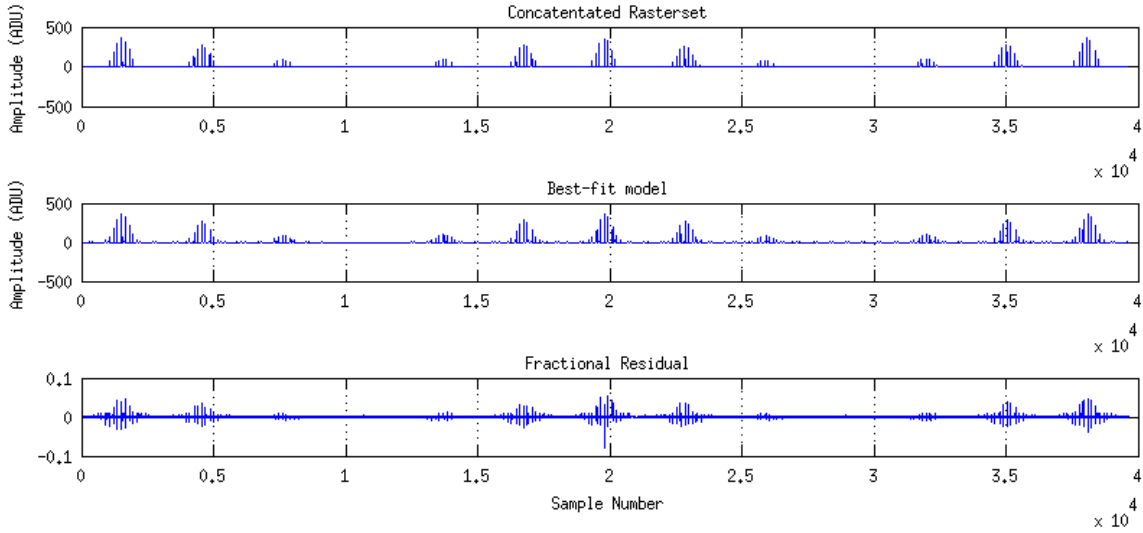
is fit to each raster,  $i$ , in a raster set where  $A_{0,i}$  is a per-raster beam amplitude,  $x_0, y_0$  is the beam center and

$$\Sigma = \begin{bmatrix} \sigma_x^2 & \rho\sigma_x\sigma_y \\ \rho\sigma_x\sigma_y & \sigma_y^2 \end{bmatrix} \quad (32)$$

where  $\sigma_x, \sigma_y$  are the beam widths in the  $x$  and  $y$  direction respectively and  $\rho$  is the correlation coefficient.

For a given detector, beam maps of all rasters in a raster set are fit simultaneously so that only one of each parameter in the exponential of Eq. 31 is estimated across all beams while the amplitude is estimated for each beam (Fig. 13). This fitting process was chosen over fitting beams separately as systematics such as polarization-dependent beam center offsets would average to zero over the full  $360^\circ$  rotation of the RPS. The result of this fitting process is an array of beam amplitudes, or modulation curve, as a function of RPS command angle.

**Figure 13.** (Top) Concatenated timestreams of beam maps from a full rasterset with best-fit model (middle) and fractional residuals (bottom).



### 3.7.2. Modulation Curve Model

The modulation curve produced in the previous section is modeled by the RF coupling between a polarized detector and transmitter. In addition to polarization angle and cross-polarization efficiency, the model also accounts for a number systematic effects including arbitrary misalignments of the source, offsets between the transmission of the source and the axis of rotation (called nutation offsets), plane projection of polarization, and amplitude dependence of anisotropic sources. In this section, the model is constructed beginning with an ideal case of a detector and polarized source perfectly coupled. From there, the model is increased in complexity by including a series of rotations from ideal representing physical misalignments during the construction and deployment of the source.

Using the nomenclature defined in §3.1, we begin by defining the ideal sensitivity a detector as represented by its polarization axis,  $\hat{D}_p$ , with angle  $\phi_d$  from the local orientation vectors:

$$\hat{D}_p(\phi_d) = \hat{D}_1 \cos \phi_d - \hat{D}_2 \sin \phi_d \quad (33)$$

In reality, any given detector may have some imperfect cross-polar leakage,  $\epsilon$ :

$$\hat{D}_p(\phi_d) = \left( \hat{D}_1 \cos \phi_d - \hat{D}_2 \sin \phi_d \right) + \epsilon \left( \hat{D}_1 \sin \phi_d - \hat{D}_2 \cos \phi_d \right) \quad (34)$$

A source at an arbitrary location is given as  $\vec{S}$  with a local coordinate system  $(\hat{x}', \hat{y}', \hat{z}')$ . For clarity, primed variables are used to denote vectors in the source's local coordinates and un-primed variables to denote vectors as they are projected onto the focal plane.

The transmission direction of the source is defined as  $\hat{S}'_t$  which lies in the direction of  $\hat{z}'$  with a copolar axis  $\hat{S}'_p$  that rotates about  $\hat{z}'$  in the  $\hat{x}'$ - $\hat{y}'$  plane as a function of  $\eta$ .  $\hat{y}'$  is defined in the right-handed sense (i.e.  $\hat{y}' = \hat{z}' \times \hat{x}'$ ) and  $\eta$  is measured from the  $\hat{x}'$ -axis toward the  $\hat{y}'$ -axis:

$$\hat{S}'_p(\eta) = \hat{x}' \cos(\eta) + \hat{y}' \sin(\eta) \quad (35)$$

When a detector is coupled to the source, the source co-polar axis is projected onto the plane tangent to the detector pointing:

$$\begin{aligned} \hat{S}_{p,2} &= \frac{\hat{D}_3 \times \hat{S}'_p}{|\hat{D}_3 \times \hat{S}'_p|} \\ \hat{S}_p &= \hat{S}_{p,2} \times \hat{D}_3 \end{aligned} \quad (36)$$

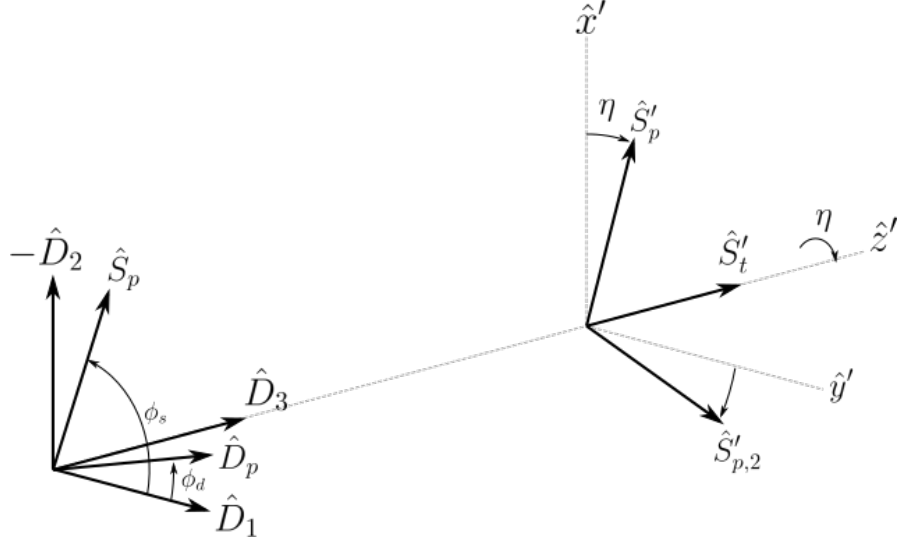
The beam of the source can also be modelled. For a source radiating isotropically, the coupling coefficient as a function of axial offset,  $\theta$ , is simply

$$A(\theta) = 1 \quad (37)$$

For the RPS, the source is modelled as a Gaussian with polar symmetry centered on  $\hat{S}'_t$  with some beam width  $\sigma$  and is peak-normalized so the coupling coefficient becomes

$$A(\theta) = e^{-\frac{1}{2}\left(\frac{\theta}{\sigma}\right)^2} \quad (38)$$

**Figure 14.** Diagram of source coordinate system in relation to detector pointing and orientation vectors.



The power measured by a detector is equal to the coupling coefficient between the source and detector and the square of the component of the electric field of polarized photons that are parallel to the detector co-polar axis

$$P = G A(\theta) |E_{\parallel}|^2 \quad (39)$$

Where  $G$  is the detector gain. The axial offset,  $\theta$ , can be calculated as

$$\theta = \cos^{-1} (\hat{S}'_t \cdot \hat{D}_3) \quad (40)$$

And the parallel component of the electric field is projection of the source polarization orientation onto the detector co-polar axis:

$$E_{\parallel} = \hat{D}_p(\phi, \epsilon) \cdot \hat{S}_p(\eta) \quad (41)$$

So the power measured by the detector becomes

$$P = G A \left( \cos^{-1} (\hat{S}'_t \cdot \hat{D}_3) \right) \left[ \hat{D}_p(\phi, \epsilon) \cdot \hat{S}_p(\eta) \right]^2 \quad (42)$$

### 3.7.3. Ideal Case

In the simplest scenario, the detector couples with a polarized source that is pointed directly at the detector and the  $\hat{x}'$ -axis, for simplicity, points along  $\hat{D}_1$ .

$$\begin{aligned}\hat{z}' \cdot \hat{D}_3 &= 1 \\ \hat{x}' \cdot \hat{D}_1 &= 1\end{aligned}\tag{43}$$

So the power at the detector becomes

$$P = G [\cos(\eta - \phi) + \epsilon \sin(\eta + \phi)]^2\tag{44}$$

### 3.7.4. Nutation Angle Offset

For rotations described in terms of Euler angles, nutation is, in the static sense, the rotation around the second Euler axis. The transmission and polarization directions of a source with a non-zero nutation angle is offset from the axis of rotation. This is modelled by using a  $z$ - $y'$ - $z''$  Euler rotation matrix  $\mathbf{M}$  to rotate the coordinate system by some nutation angle,  $a$ , in the direction of the bearing angle,  $b$ :

$$\begin{bmatrix} \hat{x}'' \\ \hat{y}'' \\ \hat{z}'' \end{bmatrix} = \mathbf{M}(-b, a, b) \begin{bmatrix} \hat{x}' \\ \hat{y}' \\ \hat{z}' \end{bmatrix}\tag{45}$$

Where  $\mathbf{M}(-b, a, b)$  is the z-y'-z'' rotation matrix which is discussed in §A.1. Because  $b$  isn't well-defined when  $a = 0$ , the basis is changed from offset and bearing to an offset in E- and H-planes by making the substitution

$$\begin{aligned}a &= \sqrt{E^2 + H^2} \\ b &= \tan^{-1} \left( \frac{E}{H} \right)\end{aligned}\tag{46}$$

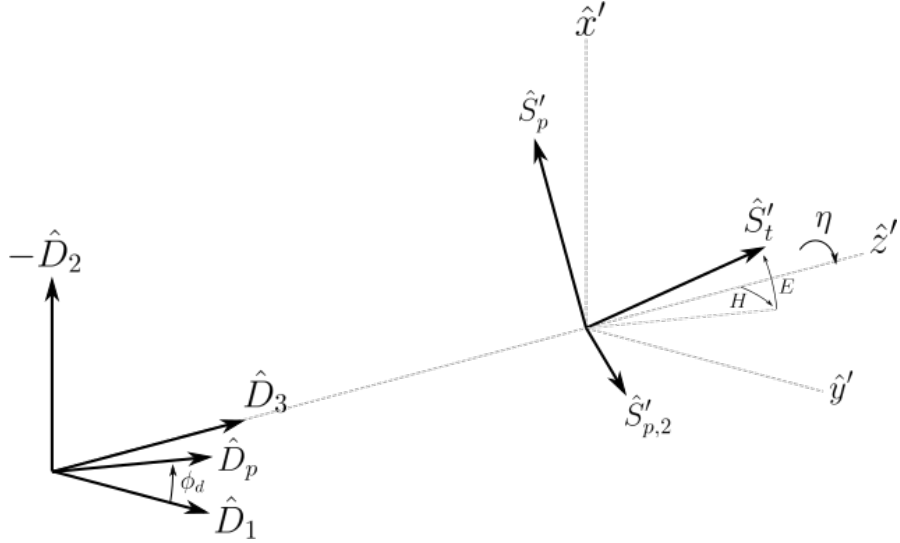


**Figure 15.** Diagram of source coordinate system in relation to detector pointing and orientation vectors.

The transmission direction and polarization orientation are then rotated about the original rotation axis,  $\hat{z}'$ , by  $\eta$ :

$$\begin{bmatrix} \hat{S}'_p \\ \hat{S}'_{p,2} \\ \hat{S}'_t \end{bmatrix} = \mathbf{R}(\eta, \hat{z}') \begin{bmatrix} \hat{x}'' \\ \hat{y}'' \\ \hat{z}'' \end{bmatrix} \quad (47)$$

Where  $\mathbf{R}$  is the Rodrigues rotation matrix about an arbitrary axis which is described in §A.2.

Then the power as readout by a detector becomes

$$P = G A \left( \cos^{-1} (\hat{S}'_t \cdot \hat{D}_3) \right) \left[ \hat{D}_p(\phi, \epsilon) \cdot \hat{S}_p(\eta, E, H) \right]^2 \quad (48)$$

### 3.7.5. Source Misalignment

The model is complicated even more when the source rotation axis is not aligned with the detector pointing.

The source coordinate system is rotated by some misalignment offset  $c$  and in the direction of bearing angle  $d$  using the same method as above.

1. Rotate about  $\hat{z}'$  by  $d$  to get  $\hat{x}', \hat{y}', \hat{z}'$

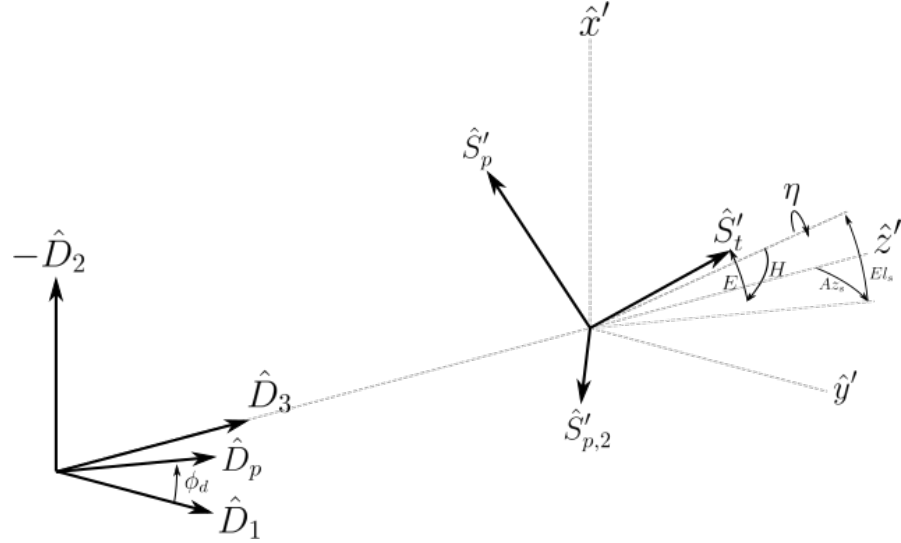


**Figure 16.** Diagram of source coordinate system in relation to detector pointing and orientation vectors.

2. Rotate about  $\hat{y}$  by  $-c$  to get  $\hat{x}'', \hat{y}'', \hat{z}''$
3. Rotate about  $\hat{z}''$  by  $-d$  to get  $\hat{x}''', \hat{y}''', \hat{z}'''$

In the case of both nutation offset and misalignment, the nutation offset is calculated first and then the entire coordinate system is rotated:

$$\begin{bmatrix} \hat{S}'_p \\ \hat{S}'_{p,2} \\ \hat{S}'_t \end{bmatrix} = \mathbf{R}(-d, \hat{z}) \mathbf{R}(c, \hat{y}) \mathbf{R}(d, \hat{z}') \mathbf{R}(\eta, \hat{z}') \mathbf{M}(-a, b, a) \begin{bmatrix} \hat{x}' \\ \hat{y}' \\ \hat{z}' \end{bmatrix} \quad (49)$$

Like the nutation offset,  $d$  is not well-defined when  $c = 0$  so the basis is changed to offsets in source Azimuth and Elevation,  $Az_s$  and  $El_s$  by substituting:

$$\begin{aligned} c &= \sqrt{Az_s^2 + El_s^2} \\ d &= \tan^{-1} \left( \frac{El_s}{Az_s} \right) \end{aligned} \quad (50)$$

Then the power as readout by the detector becomes

$$P = G A \left( \cos^{-1} \left( \hat{S}'_t(Az_s, El_s) \cdot \hat{D}_3 \right) \right) \left[ \hat{D}_p(\phi, \epsilon) \cdot \hat{S}_p(\eta, E, H, Az_s, El_s) \right]^2 \quad (51)$$

The model from Eq. 51 is fit to modulation curves estimated from beam maps. For a given detector, modulation curves from all observations, which span multiple  $DK$ -angles, were fit simultaneously to increase the number of data points used during each fit. This approach has the benefit of providing more constraining ability for nutation and alignment parameters. The parameters of  $\phi_d$ ,  $\epsilon$ , and nutation and alignment parameters were singly fit across all modulation curves while the gain,  $G$ , was estimated for each modulation curve. This accounted for the fact that, while gain variations of the source were constrained to  $< 1\%$  on raster set timescales, source gain variations between observations at different  $DK$ -rotations ( $\sim 1$  day) were not well-characterized.

During analysis, it was found that nutation and alignment nuisance parameters were poorly constrained in individual detector data even when fitting to data across all  $DK$ -angles. To maximize constraining ability, an attempt was made to fit nuisance parameters over all detector data simultaneously but proved too computationally expensive. A compromise was found by fitting over subsets of detectors (Fig. 17) which produced a distribution of nuisance parameter estimations. Then, detector polarization parameters were re-estimated individually using the mean of nuisance parameters estimations, weighted by the variance of their fit residuals, as constants during the second round of fitting.

### 3.8. Stokes Q Polarization Angle

During actual CMB observations, the timestreams of co-located A and B polarization detectors are differenced in order to fully observe in stokes Q. Thus, after  $\phi_d$ 's are estimated for all detectors, the co-located pol A and pol B detectors are combined together to form a single "pair-diff" pixel that measures Q. The polarization angle of the pair-diff axis,  $\phi_Q$ , is calculated by first computing the collective response in Stokes Q and U and then computing  $\phi_Q$ .

$$\begin{aligned} Q &= \frac{\cos(2\phi_A) - \cos(2\phi_B) - \epsilon_A \cos(2\phi_A) + \epsilon_B \cos(2\phi_B)}{2 + \epsilon_A + \epsilon_B} \\ U &= \frac{\sin(2\phi_A) - \sin(2\phi_B) - \epsilon_A \sin(2\phi_A) + \epsilon_B \sin(2\phi_B)}{2 + \epsilon_A + \epsilon_B} \\ \phi_Q &= \frac{1}{2} \tan^{-1} \frac{U}{Q} \end{aligned} \quad (52)$$

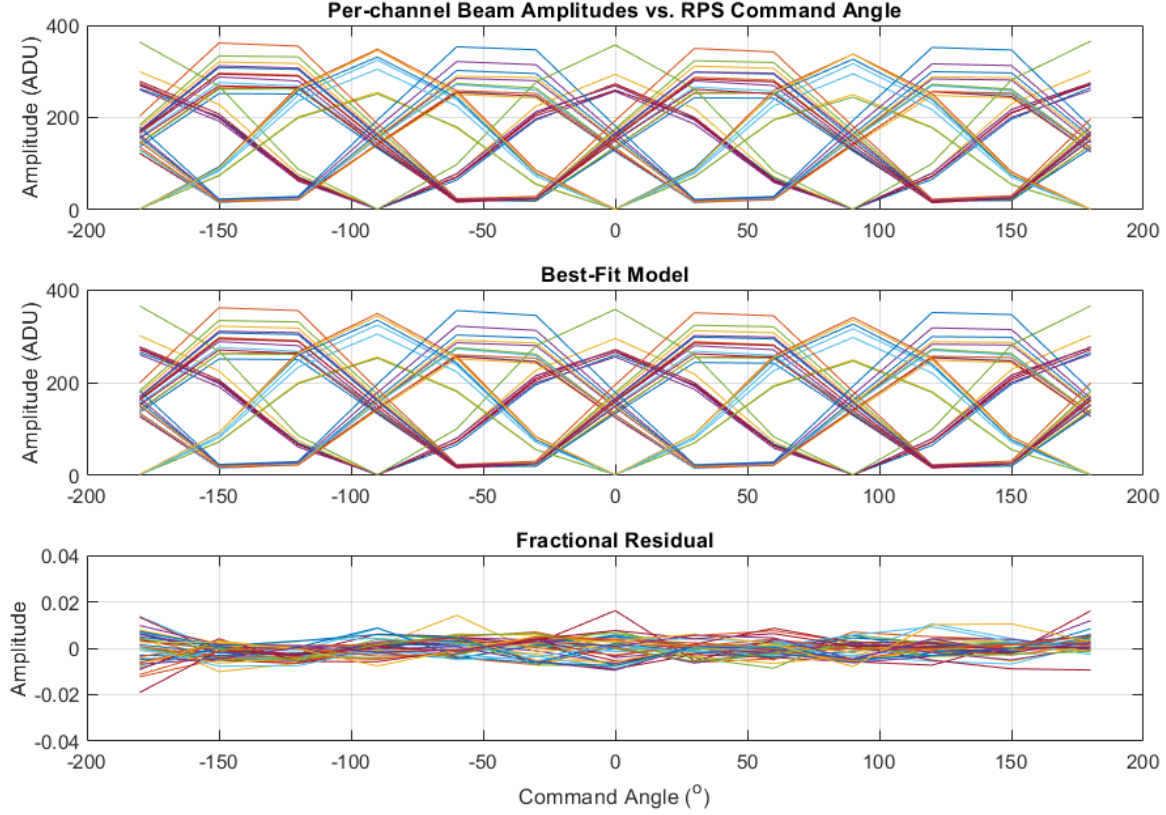


**Figure 17.** (Top) Beam-map-derived modulation curves (e.g. Fig 13) with best-fit model (middle) and fractional residuals (bottom) for a subset of detectors across multiple observations at different  $DK$ -angles.

Where  $\epsilon$  is the cross-polarization leakage of a given detector. The decision to include  $\epsilon$  in the equation above was strictly for completeness. It has been found empirically that the impact on the calculation of  $\phi_Q$  from cross-polarization leakages are negligible.

### 3.9. Uniform Rotation Angle

Finally, the uniform rotation angle of the focal plane from expected is calculated as the weighted mean of  $\phi_Q$  for all detectors on the focal plane. The intention is to estimate the effective uniform rotation angle due the the contribution of each pixel over an entire CMB observing season. The pixels are weighted by the inverse of their  $NET$ 's, a measure of their sensitivity, which is averaged over the CMB-observing season in a similar way that pair-maps contribute to coadded maps (discussed in §6).

The measured per-pixel  $NET$ 's for each scanset are averaged over a phase and then per-phase-per-pixel  $NET$ 's are averaged over all phases. Then the uniform rotation angle,  $\bar{\phi}_Q$ , is calculated as the mean of per-pixel  $\phi_Q$  which is weighted using the phase-averaged  $NET$ 's. While most channels were successfully analyzed, some measurements are missing for known good channels because the increased loading while observing at low elevation pushes these channels out of their superconducting transition regions at which point the signal from the RPS is undetectable. For known good channels without measured angles,  $\phi_Q$  is set to the tile-average during this calculation, though empirically it has been found that including these missing channels changes  $\bar{\phi}_Q$  by  $< 0.01^\circ$ .

Aside from a break over the austral summer for calibrations, BICEP3 observed the CMB uninterrupted from March 2017 through November of 2018. Analysis of observations are conventionally separated by year and so, because the telescope remained unchanged between observing seasons, two the uniform rotation angles are calculated, the first using  $NET$ 's from the 2017 CMB observing season and the second using  $NET$ 's from the 2018 CMB observing season.

### 3.10. Final Data Cuts and Consistency Checks

Upon completion of the analysis process, fit quality of each detector is examined before being included in the calculation of  $\bar{\phi}_Q$ . The per-detector fractional residuals, examples of which are shown in Fig. 17, are checked for consistency with noise using the two-sample Kolmogorov-Smirnov test. The two-sample Kolmogorov-Smirnov test is a hypothesis test which tests if two distributions are part of the same parent distribution to within an arbitrary significance ([Massey 1951](#)). The test, which is performed via a built-in MATLAB function `kstest2.m` (and is based on C-code in ([Marsaglia et al. 2003](#))), compares the distributions of best-fit residuals with a fiducial realization of noise which is representative with the parent distribution. The noise realizations have 100,000 samples, with a mean of zero and a width that is equal to the unweighted standard deviation of the difference distributions. Cases of fits in which the null hypothesis that residual distributions and noise realizations share the same parent distribution are rejected to greater than  $3\sigma$  confidence is considered a poor fit to the data and cut from the dataset.

After the final round of cuts have been completed, the data is probed for systematics by subtracting polarization angle estimations for a given detector between DK-angles. For a dataset free from systematic contamination, the resulting distributions of differences between polarization angles, dubbed difference distributions, should be Gaussian, mean-zero, and have a standard deviation equal to the square-root of two times the apparent repeatability of the measurement.

Difference distributions were checked for consistency with noise using the two-sample Kolmogorov-Smirnov test mentioned previously. However, two tests are performed on the distributions in this instance. The first test is identical to the tests above where the fiducial noise realization has a mean of zero, which is called a mean-zero test. The second test, called the mean-mean test, compares the difference distributions to a fiducial noise realization which is equal to the weighted mean of the difference distribution. The failure of the mean-zero test alone only implies an issue in the data but does not give insight to the cause. Failure of the mean-zero, but a pass of mean-mean test implies that the distribution is Gaussian, but the mean of the distribution is offset between DK-angles, which is indicative of systematics in the pointing model.

Consistency checks were performed for Pol A and Pol B angles separately and also for pair-diff angles. Their histograms are shown in Figure 18 and Figure 19. Mean-zero tests for all but one Pol A distribution and all Pol B distributions fail but most pass mean-mean tests and it is evident in Figure 18 that there exists some DK-angle dependence in polarization angle estimates on the order of  $0.2^\circ$ . Additionally, of the difference distributions that failed both tests, the common DK-angle was at  $91.25^\circ$  suggesting another systematic effect which only affected measurements taken at this DK-angle.

Similar to the tests on Pol A and pol B detectors, the pair-diff difference distributions all fail the mean-zero tests but pass the mean-mean tests. However, variation on the mean offsets from zero are reduced to  $\sim 0.1^\circ$ , which implies that the DK-dependence is greatly, but not completely, cancelled-out between Pol A and Pol B detectors.

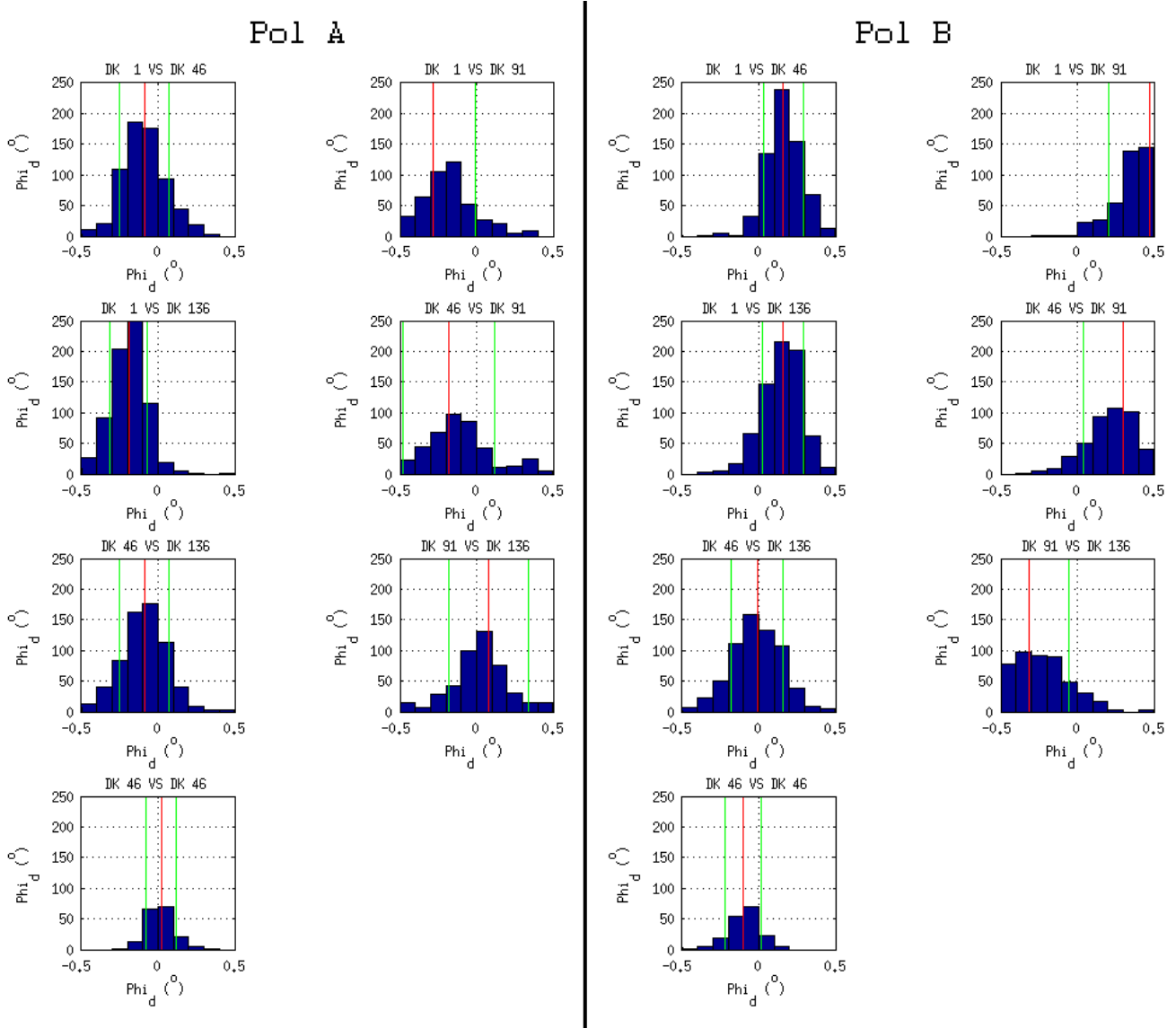


**Figure 18.** Histograms of differences between polarization angle estimations at different DK-angles, dubbed difference distributions, for Pol A and Pol B detectors (**left** and **right** respectively). Assuming no systematic effects, difference distributions should be Gaussian and mean-zero, the latter of which is clearly not the case for histograms between different DK angles. Additionally, distributions between Pol A and Pol B detectors are opposite in magnitude.

DK-Angle 1 (°)	VS. DK-Angle 2 (°)	Wt. Mean $\phi_Q$ (°)	Wt. STD $\phi_Q$ (°)	Mean-Mean Check	P-value	Mean-Zero Check	P-value
Pol A							
1.25	46.25	-0.089	0.107	Pass	0.087	Fail	$10^{-41}$
1.25	91.25	-0.254	0.178	Fail	0.000	Fail	$10^{-88}$
1.25	136.25	-0.193	0.085	Pass	0.031	Fail	$10^{-230}$
46.25	91.25	-0.164	0.174	Pass	0.124	Fail	$10^{-37}$
46.25	136.25	-0.096	0.107	Pass	0.216	Fail	$10^{-39}$
91.25	136.25	0.061	0.173	Fail	0.000	Fail	$10^{-10}$
46.25	46.25	0.021	0.072	Pass	0.024	Pass	0.010
Pol B							
1.25	46.25	0.166	0.092	Pass	0.005	Fail	$10^{-163}$
1.25	91.25	0.449	0.176	Fail	0.000	Fail	$10^{-249}$
1.25	136.25	0.159	0.094	Pass	0.103	Fail	$10^{-133}$
46.25	91.25	0.275	0.159	Fail	0.000	Fail	$10^{-108}$
46.25	136.25	-0.009	0.112	Pass	0.097	Fail	0.001
91.25	136.25	-0.297	0.180	Pass	0.005	Fail	$10^{-106}$
46.25	46.25	-0.105	0.083	Pass	0.167	Fail	$10^{-23}$

**Table 2.** Table of pair-diff difference distributions between the various combinations of DK-angles showing weighted means, weighted standard deviations, and P-values. All difference distributions pass consistency checks with mean-mean noise to within 5% significance, but fail between mean-zero consistency checks.

DK-Angle 1 (°)	VS. DK-Angle 2 (°)	Wt. Mean $\phi_Q$ (°)	Wt. STD $\phi_Q$ (°)	Mean-Mean Check	P-value	Mean-Zero Check	P-value
1.25	46.25	0.041	0.054	Pass	0.289	Fail	$10^{-22}$
1.25	91.25	0.098	0.065	Pass	0.031	Fail	$10^{-90}$
1.25	136.25	-0.020	0.062	Pass	0.037	Fail	$10^{-04}$
46.25	91.25	0.057	0.064	Pass	0.396	Fail	$10^{-29}$
46.25	136.25	-0.059	0.066	Pass	0.225	Fail	$10^{-48}$
91.25	136.25	0.121	0.070	Pass	0.325	Fail	$10^{-98}$
46.25	46.25	-0.042	0.036	Pass	0.441	Fail	$10^{-16}$

**Table 3.** Table of pair-diff difference distributions between the various combinations of DK-angles showing weighted means, weighted standard deviations, and P-values. All difference distributions pass consistency checks with mean-mean noise to within 5% significance, but fail between mean-zero consistency checks.

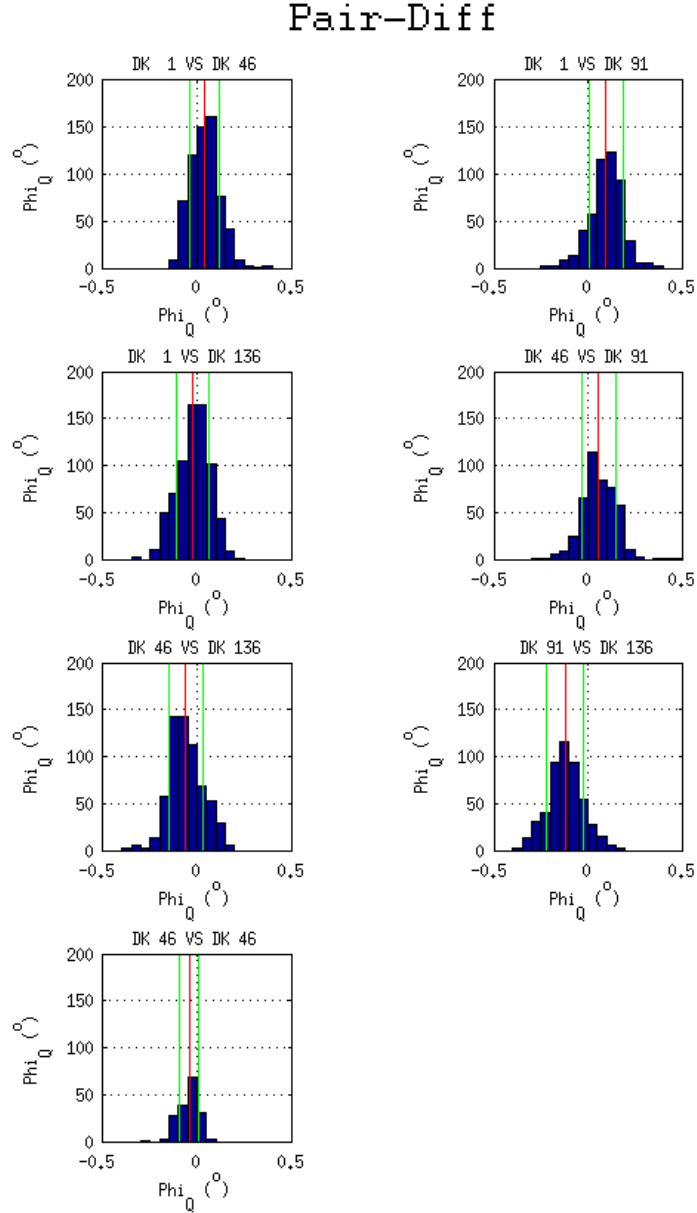


**Figure 19.** Histograms of differences between pair-diff polarization angles at different DK-angles. Unlike distributions in Fig. 18, pair-diff distributions are mean-zero in most cases to within less than a standard deviation.

### 3.11. *Propagation of Statistical and Systematic Error on $\phi_Q$*

Errors were estimated using simulations and examining the change in  $\phi_Q$  estimations. A "signal-only" modulation curve is created using dummy *Az*, *EL*, and *DK* inputs for the inverse- and beam map pointing models to return a single *x-y* coordinate which represents a beam center. The beam center, ideal polarization properties, and 13 source command angles spanning 360° are used as input into the modulation curve model which returns an idealized modulation curve. Any of the inputs to the pointing models or modulation curve model, shown in Fig. 6, can be adjusted so that the effect of a parameter can be individually .

The statistical error on  $\phi_Q$  due to stochastic fluctuations from different parts of the experiment (i.e. source power instability, rotation stage repeatability, etc...) were calculated by creating two sets of 1000 signal-only sims and dithering the amplitude (or command angle in the case of the rotation stage), where one set has an input polarization of 0° for Pol A detectors and the other set has 90° for pol B detectors. The modulation curve model is fit to the sims, assuming no dithering, and then used to compute  $\phi_Q$ . The 1- $\sigma$  standard deviation of the resulting  $\phi_Q$ 's is used as the apparent repeatability due to the error on the given parameter.

For systematic errors, two "signal-only" modulation curves are created, one with  $\phi_d = 0^\circ$  and another with  $\phi_d = 90^\circ$  representing Pol A and Pol B detectors respectively. Then for each polarization, the modulation curve model is fit but with the given input of the model adjusted by the 1- $\sigma$  error. The estimated  $\phi_d$ 's of each detector is then used to compute  $\phi_Q$ . Since the ideal  $\phi_Q$  is zero, the  $\phi_Q$  estimated as a result of the adjusted parameter is the effective 1- $\sigma$  propagated error for that parameter. The estimated impact on  $\phi_Q$  due to all the considered sources of error is tabulated in Table 4.

#### 3.11.1. *Propagation of error in Mirror and Source Parameters*

Because they are themselves estimated using beam maps, the mirror and source parameters are propagated to estimate their error in a similar fashion. Additionally, since the way in which the parameters were estimated, their errors are cumulative and so errors were propagated sequentially.

<b>Statistical Uncertainty</b>		<b>Error</b>	$\sigma(\phi_Q)$ (°)
Source Command Polarization		0.013°	< 0.01
Timestream Demodulation		2.5%	0.04
Beam Center Estimation		0.02°	< 0.01
<b>Total Statistical</b>			0.04
<b>Systematic Uncertainty</b>	<b>Input for:</b>	<b>Error</b>	$\sigma(\phi_Q)$ (°)
Azimuth Zero	IPM	0.8°	< 0.01
Elevation Zero	IPM	0.1°	< 0.01
Elevation Axis Offset <sup>†</sup>	BMPM	0.10 m	< 0.01
Mirror Tilt	BMPM	0.06°	< 0.01
Mirror Roll	BMPM	1.14°	1.60
Mirror Height <sup>†</sup>	BMPM	0.10 m	< 0.01
Source Azimuth	BMPM	1.29°	< 0.01
Source Height	BMPM	2.07 m	< 0.01
Source Distance <sup>‡</sup>	BMPM	1.00 m	< 0.01
Source Nutation E	Mod Curve Model	0.05°	< 0.01
Source Nutation H	Mod Curve Model	0.001°	< 0.01
Source Alignment Az	Mod Curve Model	1.36°	< 0.01
Source Alignment El	Mod Curve Model	0.76°	< 0.01
Wire Grid Horizontal	Mod Curve Model	0.01°	0.01
<b>Total Systematic</b>			1.61

**Table 4.** Table of sources of statistical and systematic uncertainties and their estimated impact on  $\sigma_{\phi_Q}$ . IPM and BMPM stand for inverse pointing model and beam map pointing model respectively.

<sup>†</sup> Values are acquired from as-fabricated 3D model renderings. Uncertainty is considered as a conservative upper limit.

<sup>‡</sup> Values are estimated from maps of South Pole Station layout. Uncertainty is considered as a conservative upper limit.

First, the error on mirror parameters from moon observations were calculated assuming the errors on the moon position was negligible and accounting for fluctuations on beam-center estimations and systematic error on the inverse pointing model inputs. Second, the error on the source parameters

Parameter	Statistical Error	Systematic Error
<b>Mirror (Jan '17 Moon Obs)</b>		
Tilt	0.03°	0.04°
Roll	0.07°	0.45°
<b>Source</b>		
Azimuth	0.04°	1.28°
Height	0.09 m	2.07 m
<b>Mirror (Jan '18 RPS Obs)</b>		
Tilt	0.04°	0.05°
Roll	0.01°	1.14°

**Table 5.** Table of estimated errors of the mirror and source parameters. Statistical errors limited by the repeatability on beam-center estimations and systematic error is dominated by the error on the Azimuth-zero offset due to low optical star pointing quality during the summer months. Each set of parameters use the quadrature sum of the preceding parameters' errors as input during the error propagation calculation.

was calculated using beam-center fluctuations, error on the pointing model inputs, and also with a systematic error from the mirror estimations where the quadrature sum of the statistical and systematic error was used as input. Lastly, the error on the mirror parameters were recalculated using beam-center fluctuations and error on the pointing model inputs as before but using the error on the source parameters with an additional error to account for the repeatability with which the source can be redeployed. Table 5 shows the estimated errors of the mirror and source parameters. Each set of parameters use the quadrature sum of the preceding parameters' errors as input using the error propagation calculation. In Table 4, the error of the mirror and source parameters used for propagation is the quadrature sum of their statistical and systematic uncertainties.

### 3.11.2. Final Uncertainties

The projected statistical error is confirmed by the DK45-vs-DK45 histograms in Figure 19 which is found to be 0.025°. However, the apparent scatter on  $\phi_Q$  increases to 0.045° when compared to

other DK-angles and is independent of the two DK-angles being compared. And so  $0.045^\circ$  is quoted as the statistical uncertainty for per-pixel polarization angle estimations.

As can be seen in Table 4, the modelled systematic error is dominated by the mirror's *Roll*-angle. This is due to the fact that mirror parameters are greatly affected by the error on the Azimuth-zero offset which is derived from optical star pointing, the precision of which is worse during the summer months due a lack of visible stars in the sky. Additionally, as was discussed in §3.10, there exists a still unexplained DK-dependent offset on polarization angles in the data giving a measured systematic uncertainty of  $0.1^\circ$  which, assuming the systematics due to the mirror are handled. The measured and modelled systematic uncertainties are added in quadrature for a value of  $1.61^\circ$  and is used as the total systematic uncertainty on polarization angle estimations.

## 4. RPS-DERIVED POLARIZATION PARAMETERS

### 4.1. *Per-Pixel Polarization Angles*

Using the methods described in §3.7, polarization properties for 1606 out 2640 detectors were successfully estimated comprising of 803 pixels. Fig. 20 shows a distribution of  $\phi_Q$  estimations across the BICEP3 focal plane. Tile-to-tile variation dominates on this level on the order of  $2.5^\circ$ , which is not particularly surprising as tiles are designed to be removed and installed individually and thus could be expected to have a larger margin of error for installation between tiles. When the averages of each tile is subtracted (Fig. 21), a majority of pixels appear to be randomly distributed in  $\phi_Q$  except for pixels on tile 2 and 12 which appear to have  $\phi_Q$  estimations that are dependent on their location on-tile with differences of almost  $2^\circ$ . Figure 22 shows histograms of per-tile averages of  $\phi_Q$  subtracted from all measured pixels both per-DK and DK-averaged, showing that the pixel-to-pixel variation of  $O(0.09^\circ)$  is actually a measurement of the fabrication precision.

### 4.2. *Uniform Rotation Angle*

The estimated uniform rotation angle using the per-pixel *NET*'s as weights as described in §3.9 is  $-1.15^\circ \pm 0.04^\circ(\text{stat}) \pm 1.61^\circ(\text{sys})$  for both the 2017 and 2018 CMB observing seasons where the uncertainties are the statistical and systematic uncertainties established in §3.11.2. A histogram with the uniform rotation angles overlayed are shown in Figure 23. Unfortunately, despite the high statistical precision, the uniform rotation angle is dominated entirely by the systematic error from the mirror.

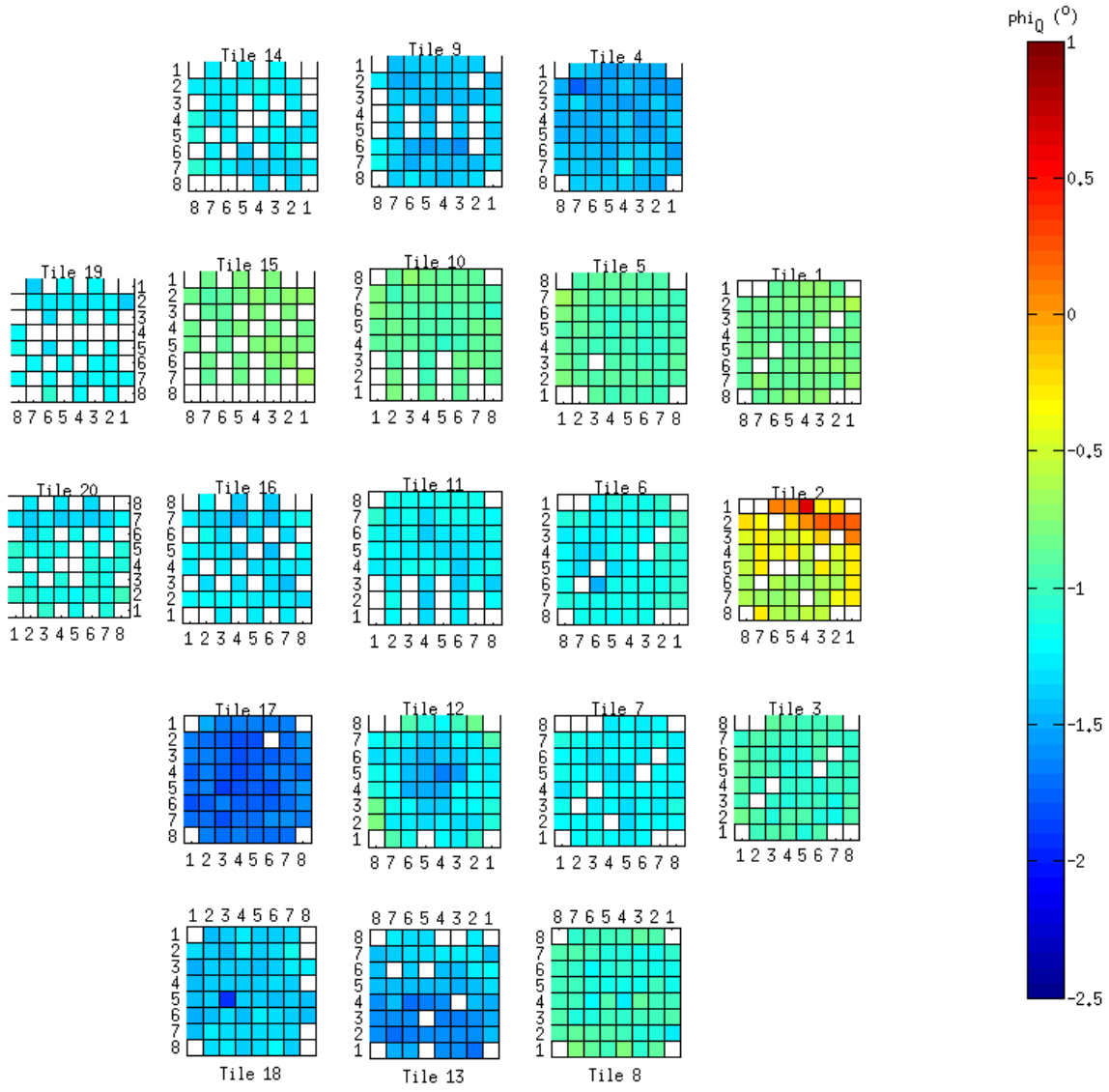


**Figure 20.** Distribution of per-pixel  $\phi_Q$  estimations based on their location on the BICEP3 focal plane.

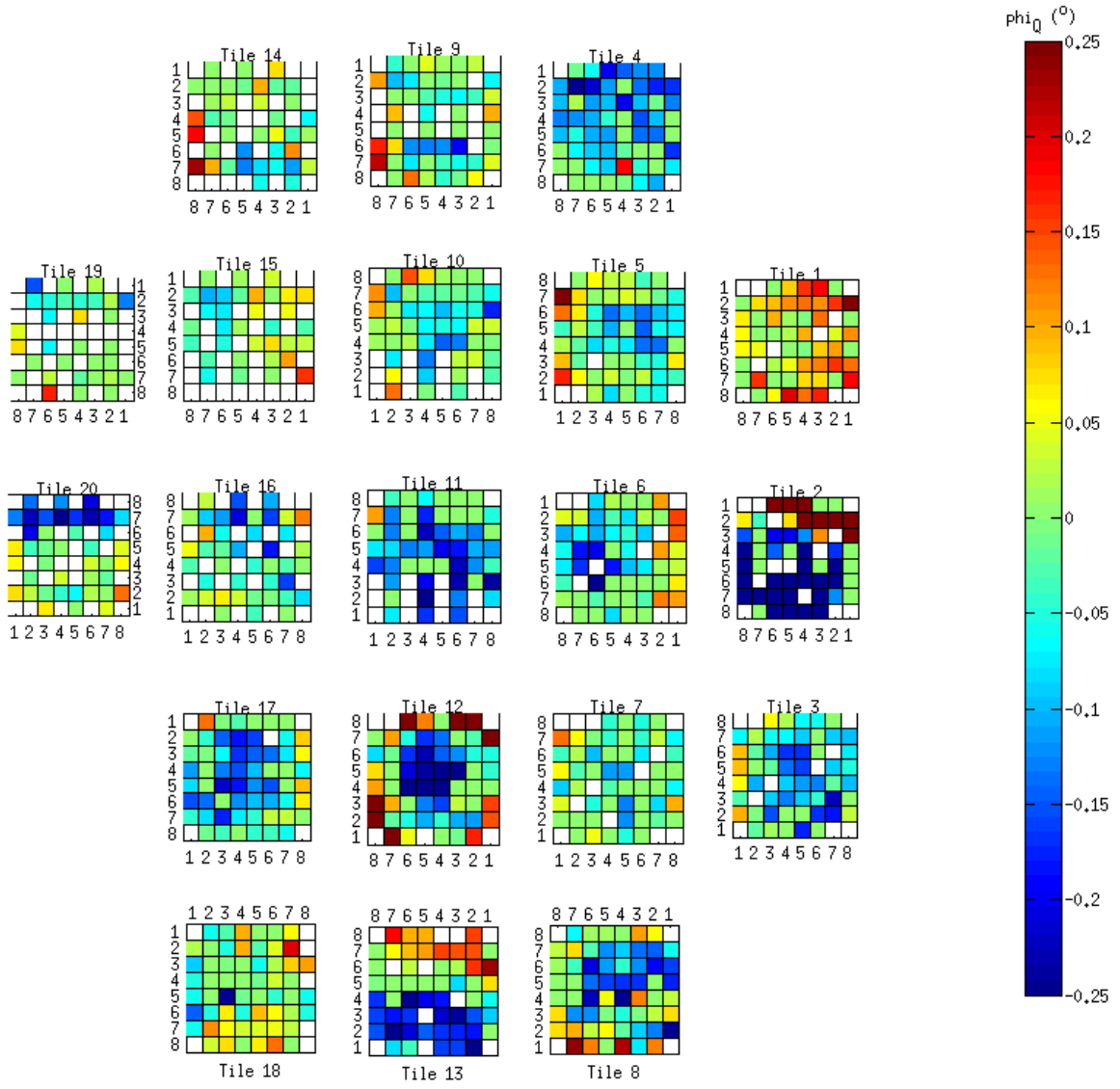


**Figure 21.** Plot of per-pixel  $\phi_Q$ , but with per-tile averages subtracted. In this plot, topographical effects intrinsic to each tile become apparent.

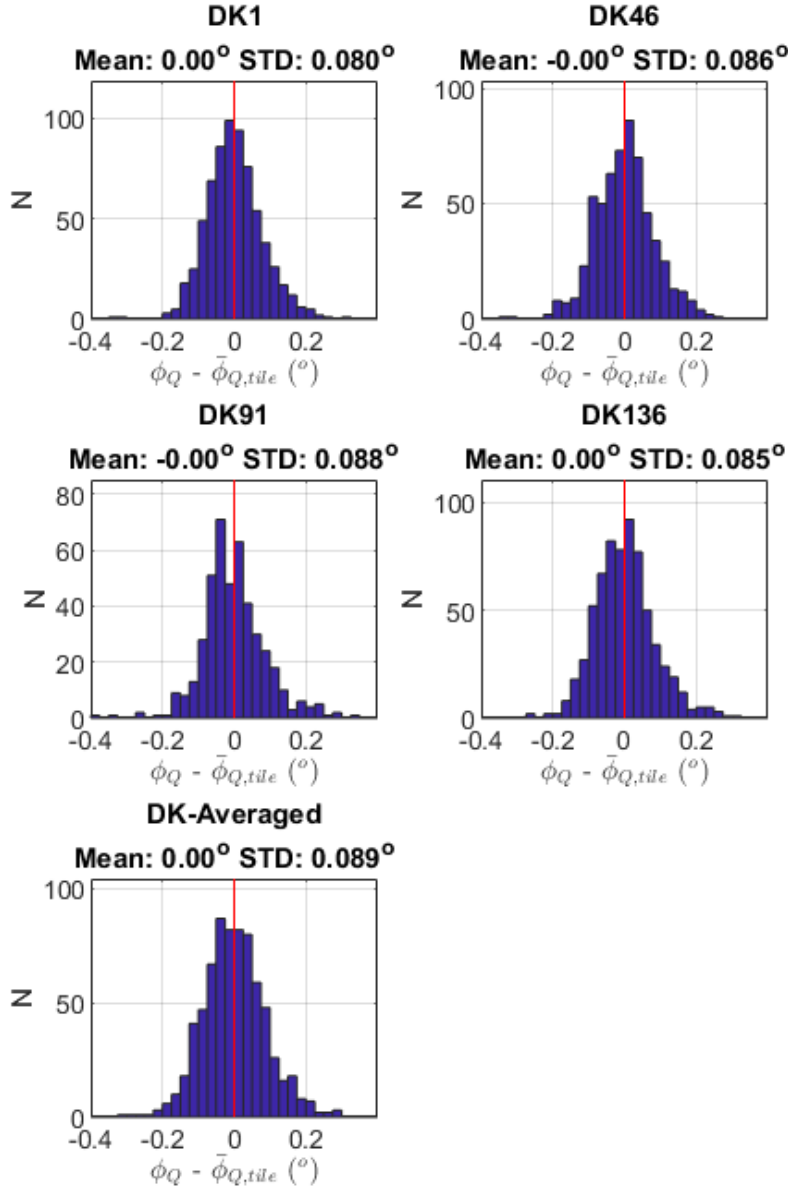


**Figure 22.** Histogram of per-tile averages of  $\phi_Q$  subtracted from all measured pixels with tiles 2 and 12 excluded shows that pixels are roughly Gaussian distributed on the order of  $0.09^\circ$ . That the pixel-to-pixel variation has converged on  $0.09^\circ$  even after averaging across DK-angles shows that this is likely a measurement of the fabrication precision.

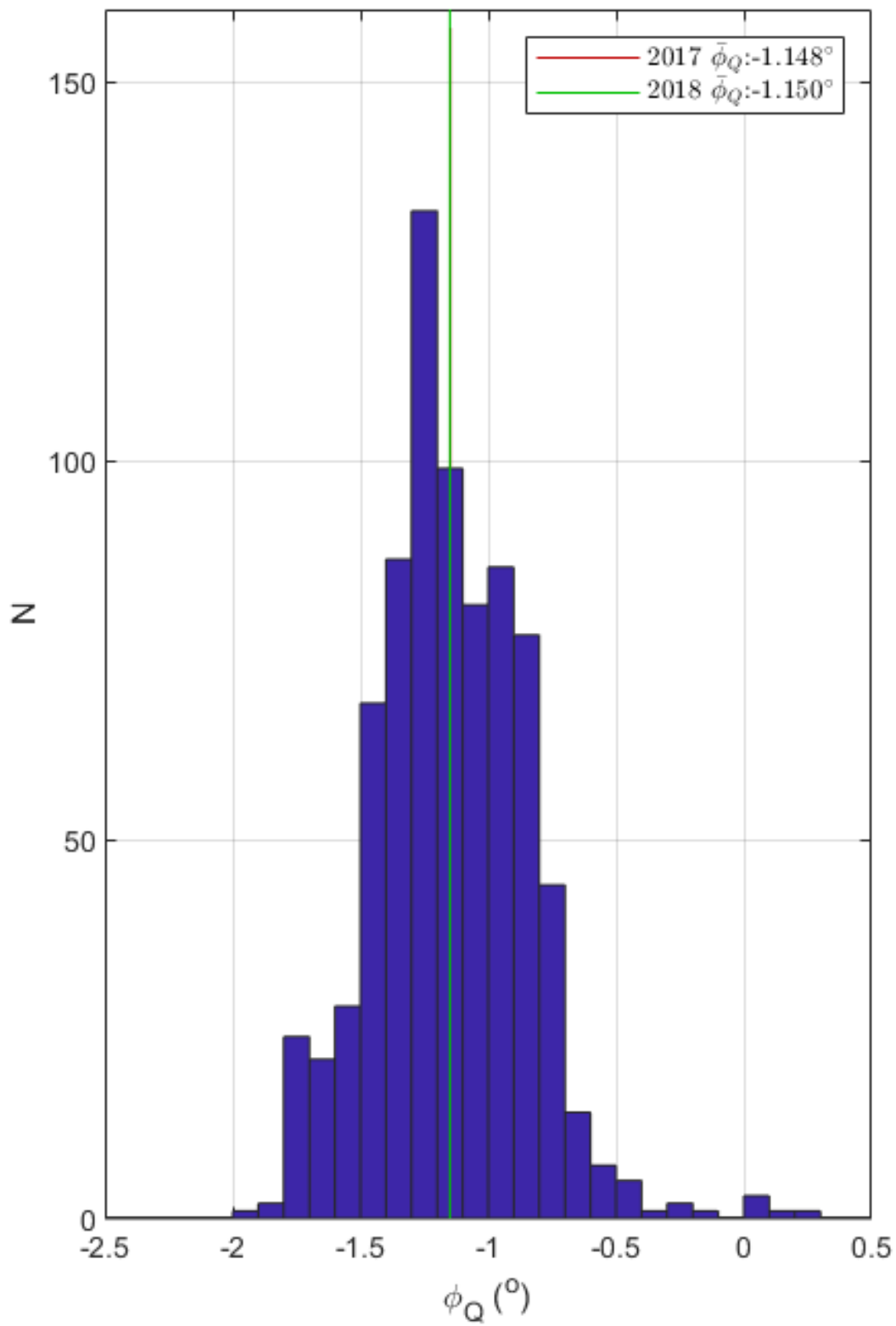


**Figure 23.** Histogram of  $\phi_Q$  estimations with  $\bar{\phi}_Q$  overlayed in red and green for 2017 and 2018 observing seasons respectively.

## 5. OTHER SYSTEMATIC CONSIDERATIONS

### 5.1. *Ground Reflections*

Demodulated timestreams of RPS data are spliced together to acquire beam maps that include ground reflections that appear at  $\sim 7$  degrees below the source elevation (Fig. 12). Ground reflections are -25dB of the source amplitude when the detectors are directly coupled to the source. A simple model is set up to estimate the contribution of ground reflections to the power measured at the source.

The total power of a 2D Gaussian is calculated with typical BICEP3 beam characteristics when it is directly coupled to a point source with an amplitude of 1. The total power is compared to the total power calculated of the same 2D Gaussian coupled to a point source of amplitude 1 with an additional point source offset by 9 degrees from the main source and with an amplitude of -25dB. The difference between the power with and without ground reflections is  $O(10^{-8})$  and the impact on parameter estimations of  $\phi_Q$  are negligible.

### 5.2. *Differential Polarization Reflection*

Using a mirror to redirect the beams of the detectors on to the horizon allows for calibration using ground-based instruments. Because the mirror, which is made of aluminum, has a large but finite refractive index, it will reflect incident light differently depending on polarization. This in turn could change the apparent polarization angle of the pixels on the focal plane as they are projected on to the source. To predict the impact of using the mirror, we first calculate the reflectivity of the mirror and then, using the beam-map pointing model to calculate the incident angle of each pixel on the mirror, we predict the effective polarization angle over the DK-angles at which the RPS was observed during the calibration season. Averaging these values together would then give us an expectation of the overall impact on differential polarization reflection on our measurements.

Using the Fresnel equations and a complex refractive index of  $n_{aL} = 2500(1+i)$  (extrapolated from IR data in (Hagemann et al. 1975)) the reflectivity of the mirror for linearly polarized light that is parallel and perpendicular to the plane of incidence can be predicted (Fig. 24).

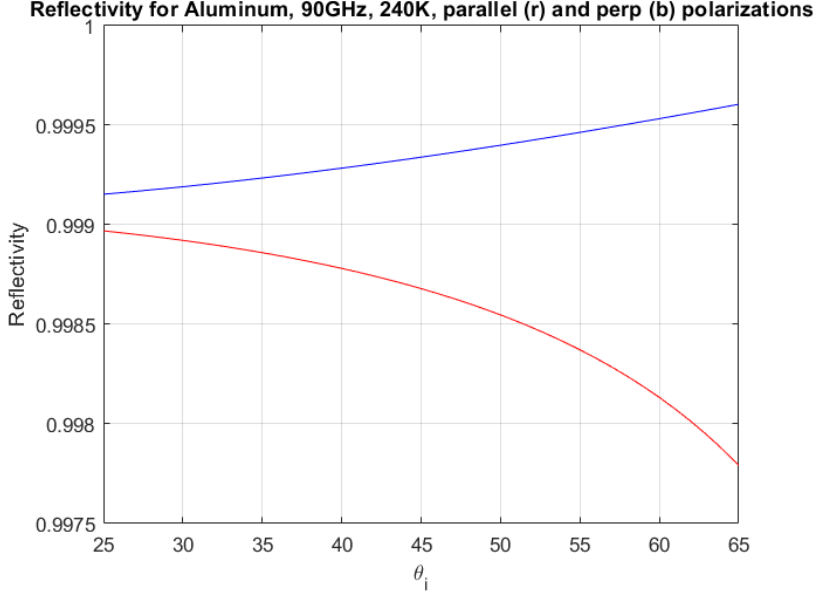


**Figure 24.** Predicted reflectivity of Aluminum as a function of incident angle,  $\theta_i$ .

Using the beam map pointing model described in §3.1, the incident angle on the mirror for a given pixel can be calculated. Figure 25 shows the incident angle on a mirror tilted 45° with respect to the telescope as a function of pixel location on the focal plane per DK-angle.

For set of A and B detectors of a given pixel with an on-FPU polarization, the apparent polarization changes due differential polarization reflection. A detector co-polar axis forms an orientation vector,  $\hat{B}_p$ , which can be separated into components,  $\hat{V}_\perp$  and  $\hat{V}_\parallel$  that are perpendicular and parallel to the plane of incidence respectively.

$$\hat{B}_p = (\hat{B}_p \cdot \hat{V}_\parallel) \hat{V}_\parallel + (\hat{B}_p \cdot \hat{V}_\perp) \hat{V}_\perp \quad (53)$$

The apparent polarization orientation due to reflection off of the mirror becomes

$$\tilde{B}_p = |r_\parallel|^2 (\hat{B}_p \cdot \hat{V}_\parallel) \hat{V}_\parallel + |r_\perp|^2 (\hat{B}_p \cdot \hat{V}_\perp) \hat{V}_\perp \quad (54)$$

where  $r_\parallel$  and  $r_\perp$  are the parallel and perpendicular reflection coefficients respectively. The effective polarization angle due to differential polarization reflection is then

$$\tilde{\phi}_p = \phi_p + \tan^{-1} \left( \frac{\hat{B}_{p,2} \cdot \tilde{B}_p}{\hat{B}_p \cdot \tilde{B}_p} \right) \quad (55)$$

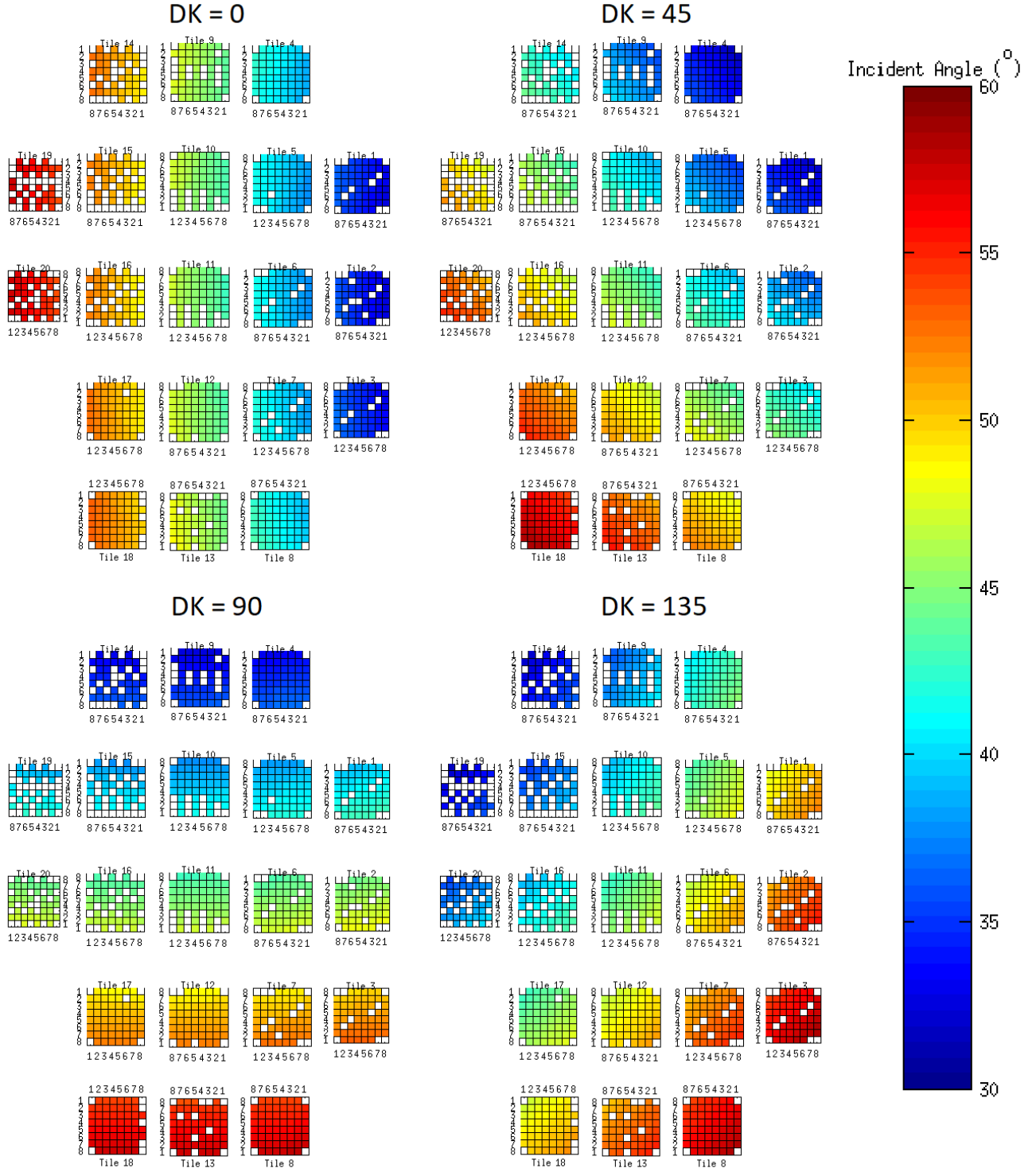


**Figure 25.** Incident angle as a function of pixel location on the focal plane per DK-angle.

Where  $\hat{B}_{p,2}$  is the basis vector that is orthonormal to  $\hat{B}_p$  and the pointing vector,  $\hat{B}_3$ , of the incident ray. For a co-located A/B pixel pair with orthogonal polarization, the effective pair-diff polarization angle becomes

$$\tilde{\phi}_Q = \frac{1}{2} (\tilde{\phi}_A + \tilde{\phi}_B - 90^\circ) \quad (56)$$

For an ideal angle of  $0^\circ$ , Figure 26 shows the bias in the pair-diff polarization angles for each pixel on the focal plane across DK-angles of  $0^\circ$  through  $135^\circ$  using the incident angles given in Fig. 25.

As seen in Figure 27, averaging across DK-angles  $0^\circ$  to  $135^\circ$  does not cancel out the bias in the pair-diff polarization angle and is on the order of  $0.01^\circ$  at the most extreme. Because this effect is an order of magnitude below the given pixel-to-pixel variation (§4), this phenomena is considered negligible for the purposes of this research.

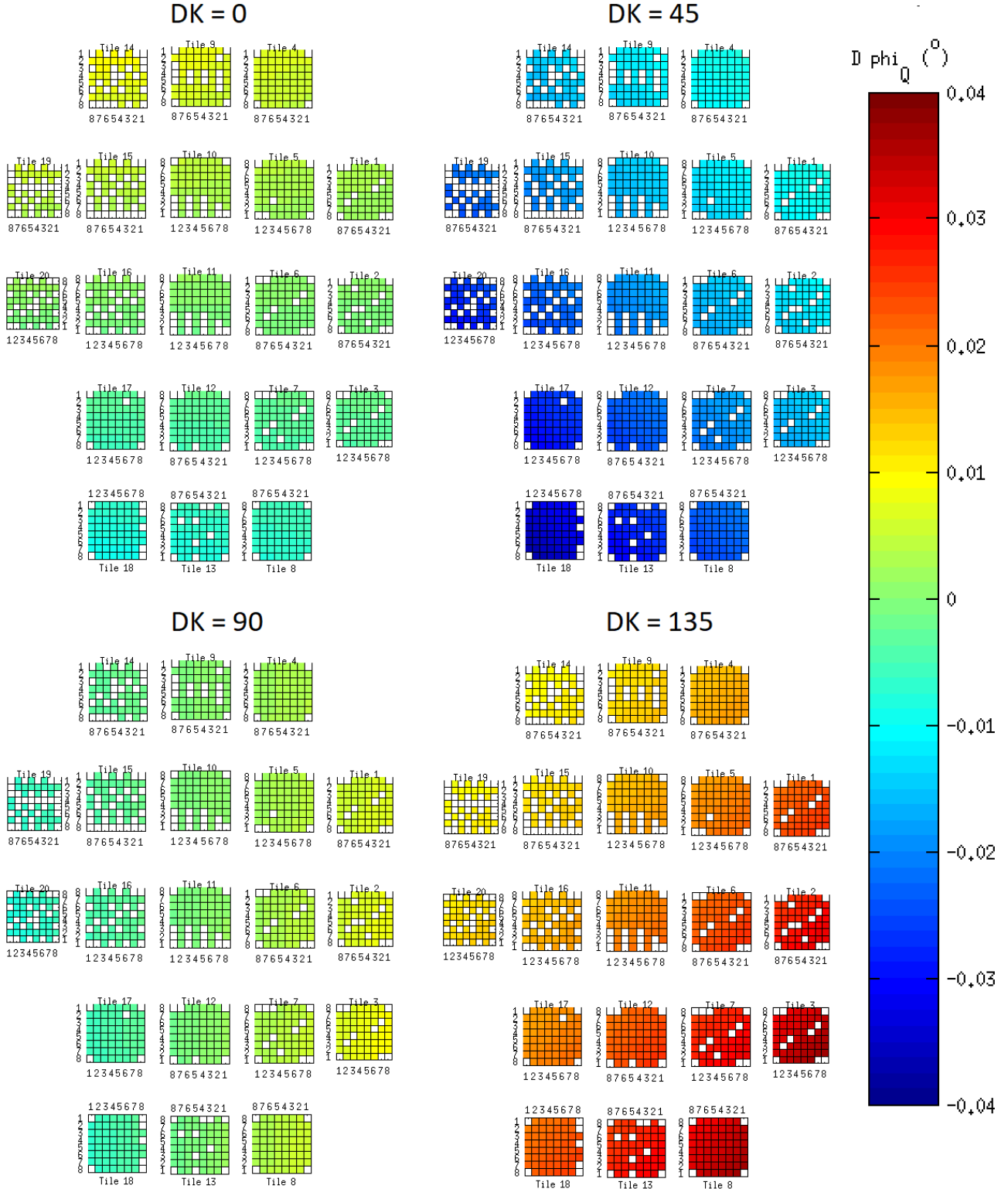


**Figure 26.** Effective change in  $\phi_Q$  due to differential polarization reflection as a function of location on the focal plane per DK-angle.

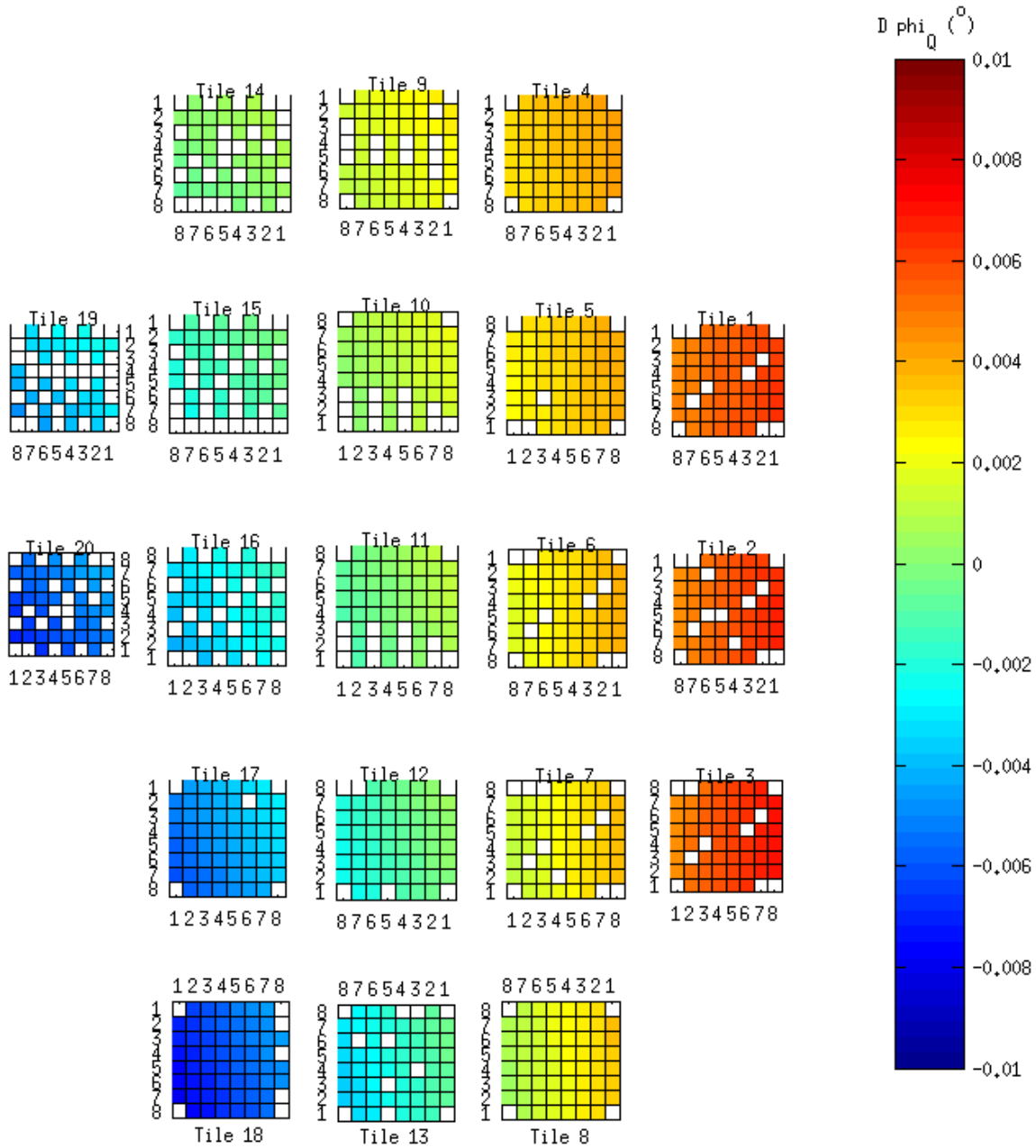


**Figure 27.** Effective change in  $\phi_Q$  due to differential polarization reflection as a function of location on the focal plane averaged across the DK-angles in Figure 26.

## 6. BICEP3 CMB OBSERVATIONS AND ANALYSIS STRATEGY

### 6.1. *Observations and Data Reduction*

Observations of the CMB for BICEP3 are conducted in a similar manner to that of the Keck Array and BICEP2 (BICEP2 Collaboration et al. 2014b, 2018). BICEP3 observes the same region of the sky as that of BICEP1, BICEP2 and Keck Array, centered at RA 0h, Dec.  $-57.5^\circ$  which lies in a region called the "Southern Hole" where polarized foregrounds are expected to be relatively low. Observations of the entire region is covered over a 3-day long schedule at a single *DK*-angle which is subdivided into eight phases with time set aside for cryogenic servicing. Of the eight phases, seven phases observe the CMB and one phase observes the galactic plane for calibration purposes. Phases are further divided into ten  $\sim 50$ -minute "scan sets" consisting of  $60^\circ$  back-and-forth scans in Azimuth with a constant Elevation and *DK*-angle stepping in  $0.25^\circ$  in Elevation between scan sets. Scan sets are deliberately made to cover a fixed range in Azimuth instead of right ascension in order to remove terrestrial signals such as local magnetic fields or optical power that is fixed with respect to the ground, and thermal fluctuations or vibrational noise that are fixed with respect to each scan (BICEP2 Collaboration et al. 2014a). Aside from a break over the austral summer for calibrations, BICEP3 observed the CMB uninterrupted from March 2017 through November of 2018. Analysis of observations are conventionally separated by year, so this report analyzes two BICEP3 data sets which span the March 2017 to November 2017 and March 2018 to November 2018 observing seasons.

The data analysis pipeline is written in MATLAB and performs some low-level reduction before the map-making process (BICEP2 Collaboration et al. 2014a). Timestream data are downsampled before they are transferred via satellite to the U.S., so first step in the reduction process is to deconvolve the filters that are applied to the timestreams. Then, glitches and flux jumps from the SQUID readout system are either corrected or flagged. The gain of each channel is then calibrated using roughly sinusoidal "nods" in Elevation (dubbed elnods) which bracket each scan set. An air-mass profile is fit to each elnod to derive the relative gain coefficient for each channel. The timestream of each channel is divided by its gain coefficient and then multiplied by the median coefficient over all "good" detectors to equalize the gain of each channel with respect to the others. The timestream

of each pair of co-located detectors are summed and differenced together for making temperature and polarization maps respectively which are then filtered to remove atmospheric  $1/f$  noise, residual magnetic pickup, and ground-fixed signals. Lastly, data is cut before and after the map-making process on a per-channel basis within scan sets based on a multitude of parameters which are used to identify spurious issues with the data ranging from poor weather to excess noise on a particular channel. While the data reduction process is fully automated, the reduced data from each scan set is manually inspected by junior members of the collaboration to identify poor-quality data that survived cuts or other issues that may arise over an observing season such as spurious increases in ground-signal pickup or vibrational noise.

### 6.2. *Map-Making and Power Spectra*

Timestreams of detector pairs are summed together (pair-sums) for temperature mapping and subtracted (pair-diffs) for polarization mapping. Pair-sum and pair-difference timestreams are binned into  $0.25^\circ$  square-pixel maps at the per-scan set, per-pair level in RA-Dec. called "pair maps" (BICEP2 Collaboration et al. 2014b). Pair maps are then accumulated over each phase at which point modes with leakage between temperature and polarization anisotropy due to beam parameter mismatches between a pair of detectors are removed in a process called deprojection (Bicep2 Collaboration et al. 2015). Coadded maps are produced by accumulating over all phases and pairs and then converted to  $T$ ,  $Q$ , and  $U$  assuming the as-designed detectors polarization orientations.

Choices in the map-making process such as timestream filtering, map projection, and apodization cause some mixing between E and B modes in the power spectra which leads to significant losses in sensitivity if not properly handled (BICEP2 Collaboration et al. 2014b). Maps of pure B-modes and E-modes are isolated from ambiguous modes via a matrix-based map purification process (BICEP2 Collaboration et al. 2016). CMB power spectra are calculated from temperature and purified maps using a method similar to that described in §1.2. Power spectra are binned into nine band powers  $\approx 35$  multipoles wide and ranging between  $20 < \ell < 340$ .

### 6.3. *Uniform Rotation Angle*

As described in §1.2, the uniform rotation angle of the CMB from the expected angle can be calculated finding a  $\Delta\psi$  such that the EB and TB cross-spectra are minimized. Within the BICEP analysis pipeline, a function exists that estimates  $\Delta\psi$  by fitting the model EB and TB cross-spectra from Eq. 12 to real band powers,  $C_{\ell,0}^{XY}$ , by minimizing the  $\chi^2$  function:

$$\chi^2 = (C_{\ell,0}^{XY} - C_\ell^{XY})^T (\mathbf{C}^{XY})^{-1} (C_{\ell,0}^{XY} - C_\ell^{XY}) \quad (57)$$

where  $\mathbf{C}^{XY}$  is the bandpower covariance matrix the construction of which is described in (Tegmark & de Oliveira-Costa 2001).

### 6.3.1. Results

The estimated uniform rotation angle for the 2017 observing season is  $-0.44 \pm 0.12(\text{stat})$  which is consistent with  $-0.40 \pm 0.12(\text{stat})$  from the 2018 observing season. The best-fit model spectrum for each season compared to the real band powers can be seen in Fig. 28.

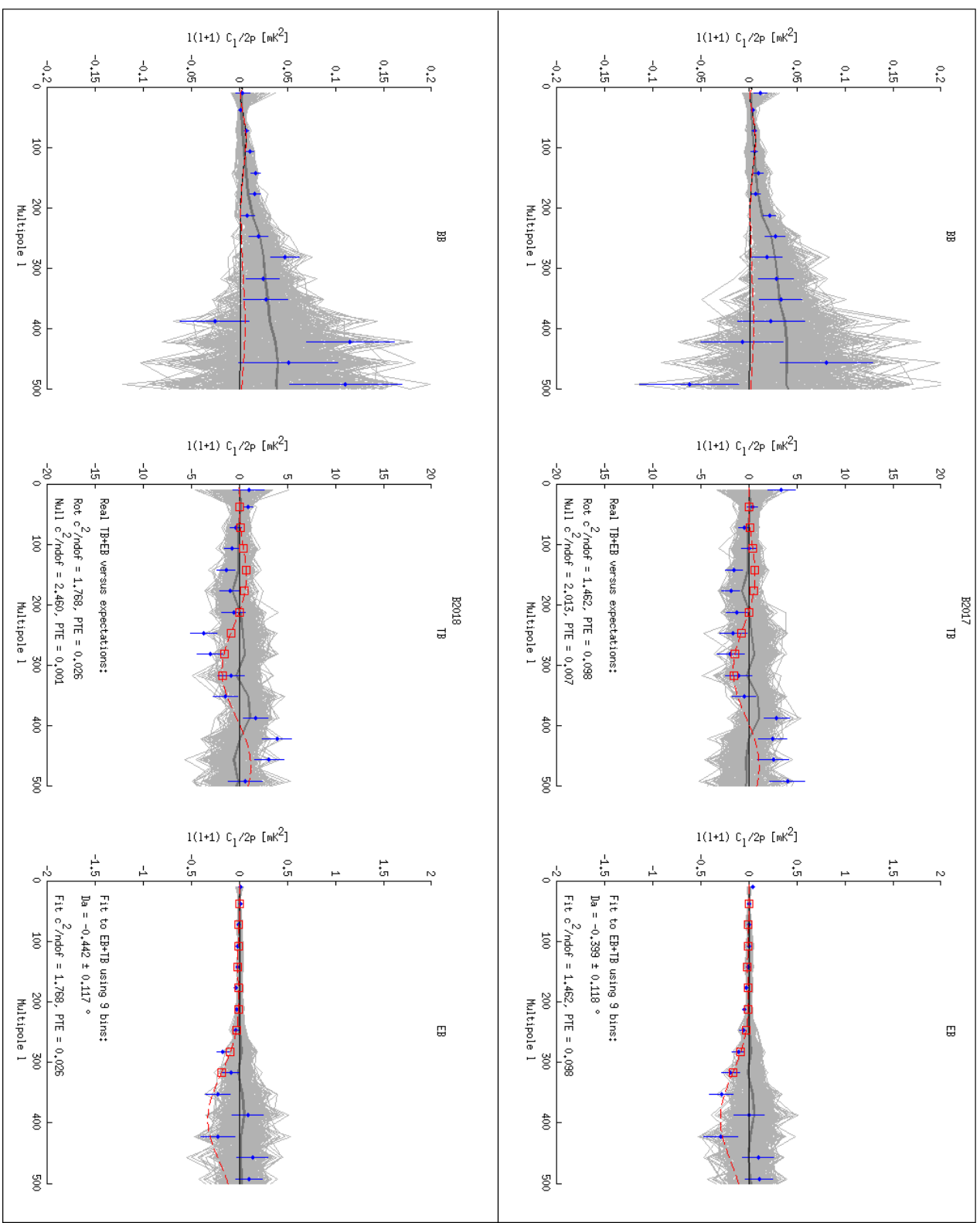


**Figure 28.** Plots of simulated and real band powers with best-fit model spectrum overlaid for BB, EB, and TB power spectra for the 2017 (top) and 2018 (bottom) observation season. Real band powers are shown in blue, model band powers are shown in red, the red dashed line is the rotated theory spectrum, the black line is the non-rotated theory spectrum, the gray lines are simulation band powers.

## 7. CONSTRAINT ON COSMIC BIREFRINGENCE

With both uniform rotation angles acquired from RPS calibrations and CMB analysis, the uniform rotation angle from Cosmic Birefringence is calculated simply from Eq. 13. The statistical uncertainty on  $\alpha$  is calculated by adding uncertainties from  $\bar{\phi}_Q$  and  $\Delta\psi$  in quadrature. Since the CMB analysis is still underway, there is currently no systematic uncertainties quoted and so only the systematic uncertainty from RPS-derived values are used. The results for the uniform rotation angles from Cosmic Birefringence are given in Table 6.

Dataset	$\Delta\psi$ (°)	$\bar{\phi}_Q$ (°)	$\alpha$ (°)
B2017	$-0.44 \pm 0.12$ (stat)	$-1.15^\circ \pm 0.04^\circ$ (stat) $\pm 1.61^\circ$ (sys)	$0.71 \pm 0.13$ (stat) $\pm 1.61^\circ$ (sys)
B2018	$-0.40 \pm 0.12$ (stat)	$-1.15^\circ \pm 0.04^\circ$ (stat) $\pm 1.61^\circ$ (sys)	$0.75 \pm 0.13$ (stat) $\pm 1.61^\circ$ (sys)

**Table 6.** Results of derived uniform polarization angles from Cosmic Birefringence by comparing BICEP3’s 2017 and 2018 observing seasons against RPS-derived uniform rotation angles.

## 8. CONCLUSIONS

A ground-based, chopped, thermal source with well known polarization properties was constructed and observed by the BICEP3 CMB Polarimeter in order to provide an independent calibration of its per-pixel polarization angles. Together the pixel’s measured polarization angles contribute to an overall polarization rotation which, when compared to the uniform rotation derived from minimizing EB and TB cross-spectra from the CMB, would provide an improved constraint on the upper limit of Cosmic Birefringence. The calibration campaign was completed over a week in late January of 2018 which allowed the measurements to be applied to CMB observations made by BICEP3 over both the 2017 and 2018 CMB observing seasons.

Much thought and effort, to great success, was put into minimizing the statistical fluctuations of the various inputs that impact our precision on polarization angle estimates; The per-pixel polarization angles were measured with a statistical error of  $0.045^\circ$ , a factor of 5 better than polarization angle measurements of the BICEP2 focal plane (BICEP2 and Keck Array Collaborations et al. 2015),

which has now surpassed the statistical precision of the uniform polarization angles estimated by the (preliminary) CMB data.

However, like previous calibration attempts, the measurement of the uniform rotation angle was dominated by systematic uncertainties due to the high sensitivity to the pointing model. The high error on the mount pointing parameters due to the low quality of the optical star pointing during summer months had an unexpectedly severe impact on the uncertainty with which the source and mirror input parameters were measured. Without the systematics due to the mirror, the measured systematic error appears to be on the order of  $0.1^\circ$ , implying that mitigating issues in the mirror would significantly improve the measurement. As such, the focus will be shifted in future work instead to better understanding the instrumental effects of the mount and developing methods which would mitigate errors on the mirror either through improved systematic control or independent consistency checks.

Fortunately, the data products of this analysis can also serve to inform the uncertainties on other aspects of the BICEP3 CMB analysis which only require knowledge of pixel angles relative to each other and not the absolute angles. For instance, the measured pixel-to-pixel variations, which were much less sensitive to the pointing model, could be used to estimate the the apparent repeatability

of tensor-to-scalar ratio estimations due to fluctuations in polarization angles across the focal plane (Bicep2 Collaboration et al. 2015).

## APPENDIX

### A. ROTATION MATRICES

#### A.1. *z-y'-z'' Euler Rotation Matrix*

The z-y'-z'' Euler Rotation Matrix is useful for parallel transporting an entire set of orthonormal basis vectors. For vectors given by  $\hat{x}$ ,  $\hat{y}$ , and  $\hat{z}$ , parallel transported in the direction of bearing angle  $\theta$  by magnitude  $r$ , the rotation can be written as:

$$\begin{bmatrix} \hat{x}''' \\ \hat{y}''' \\ \hat{z}''' \end{bmatrix} = \mathbf{M}(-\theta, r, \theta) \begin{bmatrix} \hat{x} \\ \hat{y} \\ \hat{z} \end{bmatrix} \quad (\text{A1})$$

Where  $\mathbf{M}$  is the  $\alpha$ - $\beta$ - $\gamma$  euler rotation matrix:

$$\mathbf{M}(\alpha, \beta, \gamma) = \begin{bmatrix} \cos \alpha \cos \beta \cos \gamma - \sin \alpha \sin \gamma & -\cos \alpha \cos \beta \sin \gamma - \sin \alpha \cos \gamma & \cos \alpha \sin \beta \\ \sin \alpha \cos \beta \cos \gamma + \cos \alpha \sin \gamma & -\sin \alpha \cos \beta \sin \gamma + \cos \alpha \cos \gamma & \sin \alpha \sin \beta \\ -\sin \beta \cos \gamma & \sin \beta \sin \gamma & \cos \beta \end{bmatrix} \quad (\text{A2})$$

Where the following rotations occur:

1. Rotate about  $\hat{z}$  by  $\theta$  to get  $\hat{x}$ ,  $\hat{y}$ ,  $\hat{z}$
2. Rotate about  $\hat{y}'$  by  $-r$  to get  $\hat{x}''$ ,  $\hat{y}''$ ,  $\hat{z}''$
3. Rotate about  $\hat{z}''$  by  $-\theta$  to get  $\hat{x}'''$ ,  $\hat{y}'''$ ,  $\hat{z}'''$

### A.2. Rodrigues Formula

An arbitrary vector  $\vec{V}$  can be rotated about some arbitrary unit vector  $\hat{k}$  using the Rodrigues formula

$$\vec{V}_{rot} = \vec{V} \cos \theta + (\hat{k} \times \vec{V}) \sin \theta + \hat{k} (\hat{k} \cdot \vec{V}) (1 - \cos \theta) \quad (\text{A3})$$

which can be converted to matrix notation:

$$\vec{V}_{rot} = \mathbf{R}(\theta, \hat{k}) \vec{V} \quad (\text{A4})$$

where

$$\mathbf{R}(\theta, \hat{k}) = \mathbf{I} + \sin \theta \mathbf{K} + (1 - \cos \theta) \mathbf{K}^2 \quad (\text{A5})$$

where  $\mathbf{I}$  is the identity matrix and  $\mathbf{K}$  is the cross-product matrix of  $\hat{k}$ :

$$\hat{k} \times \vec{V} = \mathbf{K} \vec{V} = \begin{bmatrix} 0 & -k_3 & k_2 \\ k_3 & 0 & -k_1 \\ -k_2 & k_1 & 0 \end{bmatrix} \begin{bmatrix} V_1 \\ V_2 \\ V_3 \end{bmatrix} \quad (\text{A6})$$

## REFERENCES

- Ahmed, Z., Amiri, M., Benton, S. J., et al. 2014, in Society of Photo-Optical Instrumentation Engineers (SPIE) Conference Series, Vol. 9153, Millimeter, Submillimeter, and Far-Infrared Detectors and Instrumentation for Astronomy VII, 91531N
- Aiken, R. W. 2013, PhD thesis, California Institute of Technology
- BICEP2 and Keck Array Collaborations, Ade, P. A. R., Aikin, R. W., et al. 2015, ApJ, 806, 206
- BICEP2 Collaboration, Ade, P. A. R., Aikin, R. W., et al. 2014a, ApJ, 792, 62  
—. 2014b, PhRvL, 112, 241101
- Bicep2 Collaboration, Ade, P. A. R., Aikin, R. W., et al. 2015, ApJ, 814, 110
- BICEP2 Collaboration, Keck Array Collaboration, Ade, P. A. R., et al. 2016, ApJ, 825, 66  
—. 2018, PhRvL, 121, 221301
- Bradford, K. J. 2012, undergraduate Thesis, Harvard University
- Carroll, S. M., Field, G. B., & Jackiw, R. 1990, PhRvD, 41, 1231
- Finelli, F., & Galaverni, M. 2009, PhRvD, 79, 063002
- Hagemann, H.-J., Gudat, W., & Kunz, C. 1975, J. Opt. Soc. Am., 65, 742.  
<http://www.osapublishing.org/abstract.cfm?URI=josa-65-6-742>
- Hui, H., Ade, P. A. R., Ahmed, Z., et al. 2016, in Society of Photo-Optical Instrumentation Engineers (SPIE) Conference Series, Vol. 9914, Millimeter, Submillimeter, and Far-Infrared Detectors and Instrumentation for Astronomy VIII, 99140T
- James, F., & Goossens, M. 1998, "CERN", cERN Program Library Long Writeups.  
<https://cds.cern.ch/record/2296388>
- Kaufman, J. P., Keating, B. G., & Johnson, B. R. 2016, MNRAS, 455, 1981
- Kaufman, J. P., Miller, N. J., Shimon, M., et al. 2014, PhRvD, 89, 062006
- Keating, B. G., Shimon, M., & Yadav, A. P. S. 2013, ApJ, 762, L23
- Komatsu, E., Smith, K. M., Dunkley, J., et al. 2011, The Astrophysical Journal Supplement Series, 192, 18
- Lee, T. D., & Yang, C. N. 1956, Physical Review, 104, 254
- Marsaglia, G., Tsang, W. W., & Wang, J. 2003, Journal of Statistical Software, Articles, 8, 1.  
<https://www.jstatsoft.org/v008/i18>
- Massey, F. J. 1951, Journal of the American Statistical Association, 46, 68.  
<http://www.jstor.org/stable/2280095>
- Pagano, L., de Bernardis, P., de Troia, G., et al. 2009, PhRvD, 80, 043522
- Planck Collaboration, Aghanim, N., Ashdown, M., et al. 2016a, A&A, 596, A110

- Planck Collaboration, Adam, R., Ade, P. A. R., et al. 2016b, *A&A*, 594, A8
- Polarbear Collaboration, Ade, P. A. R., Akiba, Y., et al. 2014, *ApJ*, 794, 171
- Rosset, C., Tristram, M., Ponthieu, N., et al. 2010, *A&A*, 520, A13
- Tegmark, M., & de Oliveira-Costa, A. 2001, *PhRvD*, 64, 063001
- Wu, C. S., Ambler, E., Hayward, R. W., Hoppes, D. D., & Hudson, R. P. 1957, *Physical Review*, 105, 1413
- Wu, E. Y. S., Ade, P., Bock, J., et al. 2009, *PhRvL*, 102, 161302
- Zaldarriaga, M., & Seljak, U. 1997, *PhRvD*, 55, 1830